Estimation of ECH deposition profiles in DIII-D plasmas based on experimental observations

Slief, Jelle H.

Award date:
2021

Eindhoven University of Technology

Master's Thesis

60 EC

Estimation of ECH deposition profiles in DIII-D plasmas based on experimental observations

---

Author:
J. H. Slief
1391372

Supervisors:
Dr. ir. M. van Berkel (ESC group, DIFFER)
Dr. M. W. Brookman (DIII-D, General Atomics)
Ir. R. J. R. van Kampen (ESC group, DIFFER)

Committee members:
Prof. dr. N. J. Lopes Cardozo (STNF group, AP)
Dr. ir. J. van Dijk (EPG group, AP)
Dr. J. Citrin (STNF group, AP)
Dr. B. Bagheri (EPG group, AP)
Dr. ir. C. V. Verhoosel (ETFD group, ME)

A public thesis submitted in fulfillment of the TU/e Code of Scientific Integrity for the degree of Master of Science in

Science and Technology of Nuclear Fusion
&
Applied Physics
Plasmas and Beams master track

July 5, 2021

EINDHOVEN UNIVERSITY OF TECHNOLOGY

Abstract

Applied Physics
Plasmas and Beams master track

Science and Technology of Nuclear Fusion

Master of Science

Estimation of ECH deposition profiles in DIII-D plasmas based on experimental observations

by J. H. Sliefr

Electron Cyclotron Heating (ECH) is an important heating technique in nuclear fusion plasmas, in part because of its highly spatially localized power deposition. The width of this deposition profile is therefore an important parameter in e.g. neoclassical tearing mode (NTM) suppression. Typically, ECH deposition profiles are estimated numerically through ray tracing codes. However, estimates of the deposition profile based on experimental methods have shown that it may be up to three times broader than ray tracing estimates. To investigate how large this discrepancy is and what causes it, five different estimation methods based on experimental data are implemented and verified on simulated data before being applied to electron temperature measurements from six different DIII-D discharges.

The simulations show that break-in-slope and FFT power deposition estimates are artificially broadened in the presence of transport. The other three methods do not show artificially broadened profiles as they simultaneously estimate transport and power deposition: they estimate simulated profiles well both in the absence and presence of noise and for a variety of profile shapes. It is also shown that the accuracy of estimated transport does not influence the accuracy of the power deposition estimate.

The estimation results for the six DIII-D discharges analyzed show power deposition profiles that are between 1.0 and 6.2 times wider than TORAY-GA ray tracing profiles, with the majority of estimates between 1.5 and 3.5 times. Across the six discharges, with different experimental conditions, the observed broadening shows a positive correlation with deposition radius and a negative correlation with electron pressure at the deposition location. These correlations are still preliminary but taken together with evidence from literature could hint at a significant double-pass contribution to ECH absorption in the discharges analyzed or a pressure-based physical process that contributes to the broadening.

Acknowledgements

Throughout this project I have received a great deal of invaluable support from many people, whom I would like to thank here.

First, I would like to acknowledge my two academic supervisors, prof. dr. Niek Lopes Cardozo and dr. ir. Jan van Dijk, for their guidance and for keeping me on track throughout the project.

I would like to express my gratitude to my supervisors at DIFFER, dr. ir. Matthijs van Berkel and ir. Ricky van Kampen. I cannot stress enough how valuable your input to this project have been. Matthijs, thank you for your great and continued involvement in my work, your invaluable advice and your professional guidance. Ricky, thank you for mentoring me though this project and for your perpetual willingness to help me out, especially in helping me solve practical issues but also in thinking along.

I am grateful for the help of dr. Michael Brookman, without whom I could not have done this work. Mike, thank you for taking so much of your time to help me sort things out and to discuss my work, from halfway across the globe.

In addition to direct supervisors, I would like to thank the many people at DIFFER for valuable discussions and feedback on my work. In particular, prof. dr. Marco de Baar, dr. Egbert Westerhof, dr. Jonathan Citrin and his group, Garud Snoep, and the members of the ESC group at DIFFER: Jesse Koenders, Thomas Bosman, Jelle de Vries, Bart van den Boorn, Gijs Derks, Bob Kool and Andreas Waldus. I thank you all for your valuable input.

I would like to extend my gratitude to my parents and my sister for their support and creative input. I thank Daniel, Maria and Michael for their input and their help, especially in putting things into perspective.

Finally, thank you to Maria João for keeping me sane.

Contents

List of Abbreviations

BIS	**B**reak-**I**n-**S**lope
DFT	**D**iscrete **F**ourier **T**ransform
DT	**D**euterium **T**ritium
ECCD	**E**lectron **C**yclotron **C**urrent **D**rive
ECE	**E**lectron **C**yclotron **E**mission
ECH	**E**lectron **C**yclotron **H**eating
ELM	**E**dge **L**ocalized **M**ode
FDLS	**F**requency **D**omain **L**east **S**quares
FF	**F**lux **F**it
FFT	**F**ast **F**ourier **T**ransform
FWHM	**F**ull **W**idth at **H**alf **M**aximum
GHG	**G**reen **H**ouse **G**as
H-mode	**H**igh confinement mode
HFS	**H**igh **F**ield **S**ide
L-mode	**L**ow confinement mode
LCFS	**L**ast **C**losed **F**lux **S**urface
LFS	**L**ow **F**ield **S**ide
LPM	**L**ocal **P**olynomial **M**ethod
MECH	**M**odulated **ECH**
MHD	**M**agneto**H**ydro**D**ynamics
MLE	**M**aximum **L**ikelihood **E**stimator
MLEn	**MLE** for **n** points
NBI	**N**eutral **B**eam **I**njection
NTM	**N**eoclassical **T**earing **Mode**
ODE	**O**rdinary **D**ifferential **E**quation
ODR	**O**rthogonal **D**istance **R**egression
PDE	**P**artial **D**ifferential **E**quation
RF	**R**adio **F**requency
SNR	**S**ignal-to-**N**oise **R**atio
SSE	**S**um of **S**quared **E**rrors
TLS	**T**otal **L**east **S**quares
QH-mode	**Q**uiescent **H**-mode

Physical Constants

Speed of light in vacuum[1]	$c = 2.997\,924\,58 \times 10^{8}\,\mathrm{m\,s^{-1}}$ (exact)
Boltzmann constant	$k_B = 1.380\,649 \times 10^{-23}\,\mathrm{J\,K^{-1}}$ (exact)
Elementary charge	$e = 1.602\,176\,634 \times 10^{-19}\,\mathrm{C}$ (exact)
Planck constant	$h = 6.626\,070\,15 \times 10^{-34}\,\mathrm{J\,Hz^{-1}}$ (exact)
Electron rest mass [2]	$m_e = 9.109\,383\,701\,5(28) \times 10^{-31}\,\mathrm{kg}$
Proton rest mass [3]	$m_p = 1.672\,621\,923\,69(51) \times 10^{-27}\,\mathrm{kg}$
Vacuum permittivity [4]	$\epsilon_0 = 8.854\,187\,812\,8(13) \times 10^{-12}\,\mathrm{F\,m^{-1}}$
Imaginary unit (squared)	$i^2 = -1$

[1] All physical constants are defined according to the 2019 redefinition of SI base-units [1]

Chapter 1

Introduction

To feed a growing energy demand [5] under the pressing constraints of global warming, which includes a drastic reduction in anthropogenic greenhouse gas (GHG) emissions [6], new, clean and renewable energy sources must be, and are, developed and deployed.

Nuclear fusion is one such energy source currently under development. Its potential as a renewable energy technology is great: virtually no GHG emissions, no intermittency issues, no dependence on environmental conditions, no long-lived radioactive waste and no danger of explosive runaway reactions, fueled by the most abundant element on earth, with the potential for large-output and compact reactors akin to modern coal-fired and fission plants.

An important heating technique in nuclear fusion devices is electron cyclotron heating (ECH), injecting electromagnetic radiation in the electron cyclotron (EC) frequency range [7, 8]. For many ECH applications, the highly spatially localized power deposition of the millimeter-wavelength EC waves is a crucial feature [7–12]. This is true in particular for the stabilization of neoclassical tearing modes, a class of instabilities in tokamaks with the potential to disrupt the fusion process and damage the reactor [13–16].

In the last two decades, however, observations in various experimental fusion devices have suggested that the ECH deposition profile is significantly wider than previously thought [17–20]. Experimentally observed broadening up to 2-3 times compared to theoretical estimates have been observed in the DIII-D tokamak [21–26]. This discrepancy between theoretical estimations and experimental observation must be resolved. To contribute to settling this issue, this research will target the following question:
How large is the discrepancy between theoretical and experimental estimates of the ECH power deposition profile in DIII-D plasmas and what causes it?

This question will be answered by applying several different power deposition profile estimation methods to time-resolved electron temperature measurements from perturbative ECH experiments done in DIII-D, and comparing them to one another and to ray tracing estimates. The estimations based on experimental methods that have historically been employed to determine deposition profiles neglect transport, which can obscure the base deposition profile and artificially broaden its estimate in the presence of significant levels of transport [27]. This work will compare these methods against recently developed methods that simultaneously estimate power deposition and transport coefficients [27–32]. In this way, we hope to get an accurate estimation of the physical deposition profile, use this to check whether ray tracing underestimates deposition width, and, in what circumstances.

The structure of this thesis is as follows: in chapter 2, the terminology specific to nuclear fusion will be elaborated on and the necessary theoretical background for understanding this work will be provided. In chapter 3, the implementation of two estimation methods is detailed and in chapter 4, these and two others are validated against simulations. In chapter 5, estimated deposition profiles will be presented for various DIII-D discharges, as well as possible scalings of broadening. Chapter 6 contains a discussion of all results and an outlook for future work and chapter 7 concludes.

Chapter 2

Background: Nuclear Fusion, ECH and Deposition Profile Estimation Techniques

This chapter collects all background information relevant to the subsequent chapters in this thesis. Sections 2.1 - 2.3 will explain nuclear fusion, tokamaks and their magnetic field configuration, and the details of electron cyclotron heating and emission. Section 2.4 will discuss the DIII-D tokamak and its diagnostics, section 2.5 will explain perturbative experiments and the transport equation, and section 2.6 will present the deposition profile estimation methods that will be employed throughout the rest of the thesis.

For the reader with extensive knowledge of nuclear fusion, some sections in this chapter may contain redundant information; they may wish to skip these sections and start e.g. at sections 2.4, 2.5 or 2.6. Sections 2.1 - 2.3 will contain relevant information for the physicist without fusion expertise, for whom this thesis is also written.

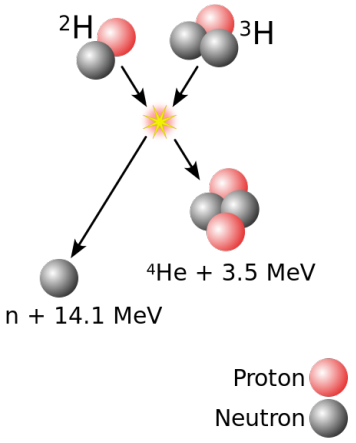

FIGURE 2.1: The fusion reaction (schematically depicted) between deuterium (^{2}H or D) and tritium (^{3}H or T) releases 17.6 MeV of energy, spread over a 3.5 MeV alpha particle and a 14.1 MeV neutron. Most nuclear fusion energy reactor designs employ this reaction because of its large cross-section, large energy release, and one of its products being charged allowing for a self-sustained reaction.

2.1 Nuclear Fusion

Nuclear fusion is the process in which atomic nuclei fuse together to form new nuclei. This process occurs when the reacting nuclei are brought together close enough for the coulomb barrier between the two to be overcome and the strong nuclear force to bind the nuclei into a new nucleus [33]. For light elements, this process releases astronomical amounts of energy. Under the right conditions, this energy can be harnessed and converted into electricity [34].

In the sun, which generates its energy through the fusion process, the immense gravity in the core of the star provides much of the energy needed to make the fusion process happen. On Earth, this gravitational pressure cannot be utilized, and thus the energy needed for the reactants to overcome the Coulomb barrier needs to be supplied through other means. In the most promising reactor designs, this is done by heating the fuel, consisting of a 50/50 mixture of hydrogen isotopes deuterium (D) and tritium (T) to temperatures of approximately 160×10^6 K, at which point the fuel is fully ionized (i.e. a plasma) and a significant fraction of the ions have sufficient energy to tunnel through or overcome the Coulomb barrier and fuse to produce 17.6 MeV of energy per reaction (figure 2.1). For reference, burning a single octane molecule (one of the main combustible materials in gasoline) releases just under 50 eV of energy, a *six orders of magnitude* less than the DT reaction [34]. The DT reaction is chosen in most reactor designs because it has the largest reaction

rate at the lowest temperature; other fuels would need to be heated to even more extreme temperatures while producing fewer reactions without compensating with a larger energy release per reaction [34].

Some the most promising candidate reactor designs for fusion energy production rely on magnetic confinement of the plasma to balance its thermal pressure. The charged fusion products (alpha particles in the case of DT fusion) are confined with the fuel and help to sustain the reaction by resupplying their energy to the fuel, while the non-charged products (neutrons) escape the fuel for their energy to be harvested and converted to electricity. Moreover, in the case of DT fusion, the escaping neutrons are not only harvested for energy but also to generate new tritium to be used as fuel [34, 35]. The leading candidate design in magnetic confinement fusion is the tokamak [36].

2.2 Tokamaks

The tokamak reactor has a toroidal reactor vessel from which it derives its name [37]. Large magnetic coils surround the reactor vessel and a large central solenoid drives a current through the plasma in toroidal direction. Together, the coils and the current generate the electric field needed to confine the plasma inside the reactor vessel (figure 2.2).

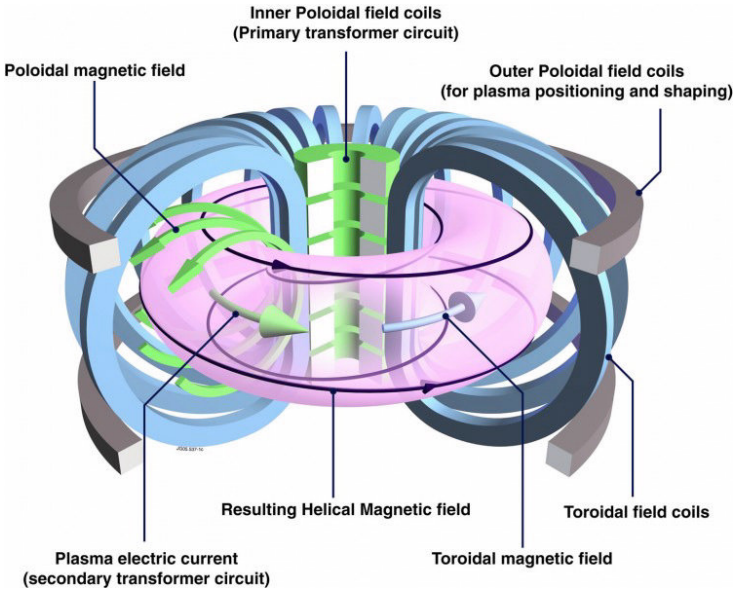

FIGURE 2.2: The tokamak consists of three main sets of coils: the D-shaped toroidal field coils (blue) that cause the toroidal magnetic field (blue arrow); the central solenoid (green) that drives the plasma current (green arrow inside the pink plasma), which in turn produces the poloidal magnetic field (green arrows around the pink plasma), which in combination with the toroidal magnetic field results in a helical field (black arrows); and the poloidal field coils used for plasma shaping and positioning [38].

In tokamaks, the toroidal component of the magnetic field is generated by the large D-shaped coils (depicted in light blue in figure 2.2). Due to the toroidal geometry the the toroidal field coils are spaced closer together on the inside of the torus and spaced further apart at the outside. This causes the toroidal magnetic field strength B_ϕ and, because that is by about an order of magnitude the largest field component, approximately the overall magnetic field strength B to decrease radially outward, inversely proportional to the major radius R of the machine:

$$B \approx B_\phi = B_0 \frac{R_0}{R}, \tag{2.1}$$

where B_0 is the toroidal field strength at the location $R = R_0$ (figure 2.3). R_0 denotes the approximate center of the vacuum vessel, the major radius of the device. It is also typically the approximate location of the plasma magnetic axis.

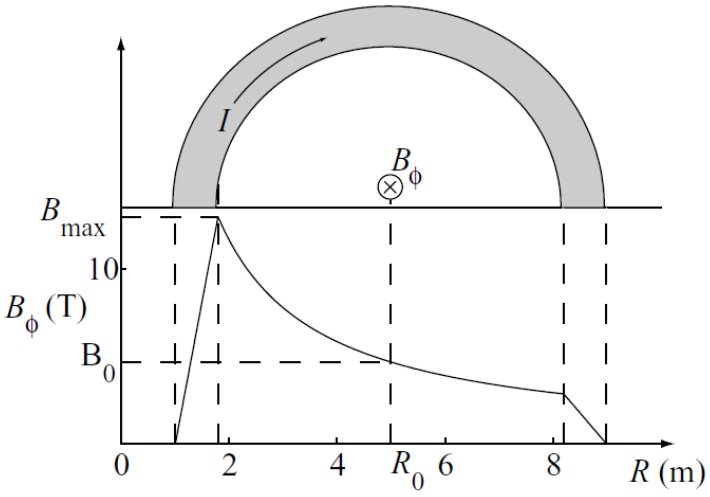

FIGURE 2.3: The arrangement of toroidal field coils (schematically depicted in gray in the top half of the figure) around a tokamak with the direction of its current I results in a magnetic field inside the coil whose field decreases with a1/R dependence [34].

2.2.1 Magnetic field structure

The tokamak and its plasma are axisymmetric, so processes in the plasma tend to be independent of toroidal angle and can be reduced to a two-dimensional description in the poloidal plane.

Due to the arrangement of coils and the plasma current in a tokamak, field lines arrange themselves in a special topology: they lie on nested toroidal surfaces [39]. A visualization of these flux surfaces is show in blue in figure 2.4 for the DIII-D tokamak. Because charged particles move freely along field lines lying on these surfaces but not across them, many properties of the plasma (such as density and temperature) rapidly equilibrate and are essentially constant over these surfaces. Therefore, the two-dimensional treatment of plasma parameters can be reduced further to a single dimension: radially outward from the magnetic axis. This one-dimensional coordinate is the flux surface label (figure 2.4), defined such that it has value 0 at the magnetic axis and 1 at the last closed flux surface (LCFS). In cylindrical geometry, this flux label is approximated by the normalized plasma minor radius:

$$\rho \approx \frac{r}{a}, \tag{2.2}$$

with a the plasma minor radius in m and r the minor radius coordinate with its origin at major radius R_0. This parameter ρ is very important as it is the coordinate that will be used to describe spatial dependence throughout this thesis.

2.2.2 Stabilization of Neoclassical Tearing Modes

The presence of the plasma current in tokamaks creates instabilities called neoclassical tearing modes (NTMs) [41, 42]. These NTMs allow faster-than-usual radial transport to occur, causing serious degradation of plasma energy confinement and therefore fusion performance [43]. Moreover, if these instabilities are allowed to grow in size they will eventually disrupt the fusion plasma, not only degrading but causing full loss of confinement. This potentially releases a large fraction of the stored energy in the plasma into the reactor wall, which can melt the wall and cause serious and costly damage [44]. As the energy stored in fusion plasmas will only increase for commercial grade reactors compared to present day experimental

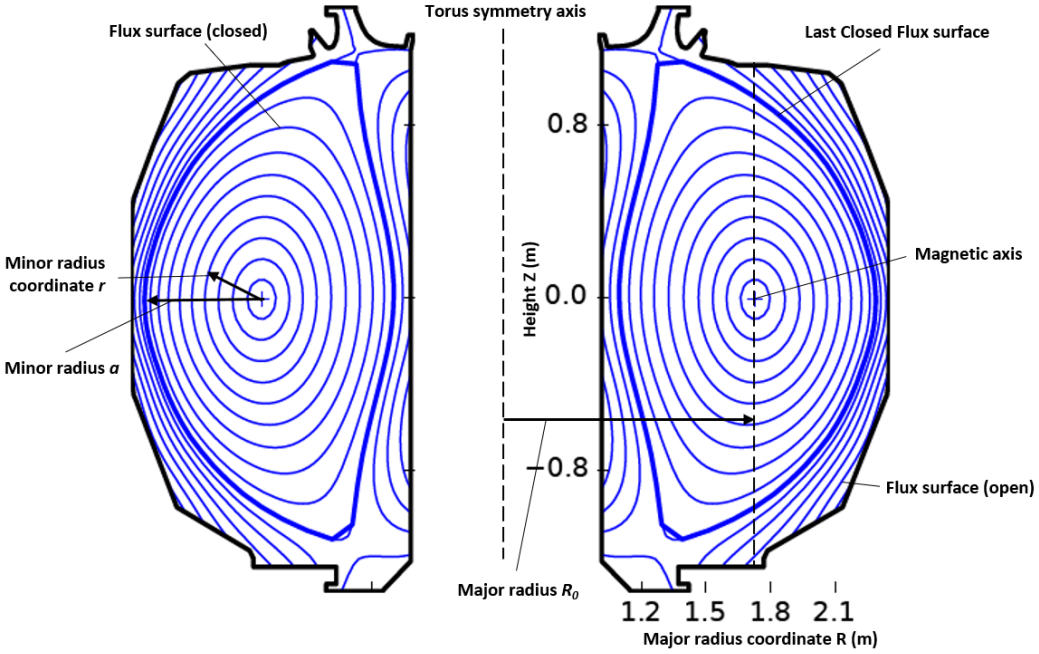

FIGURE 2.4: Reconstructed equilibrium flux surfaces (in blue) of an upper-divertor magnetic geometry in the DIII-D tokamak using the equilibrium solver EFIT [40], shown in the poloidal plane. Major and (normalized) minor radii are indicated.

devices, stabilization of these tearing modes is critical to the success of nuclear fusion as an energy technology. Using ECH (or the related technique of electron cyclotron current drive, ECCD [17]) targeted at the instability locations has been shown to stabilize them [45, 46]. Since this requires deposition of the power in the center ('O-point') of the instability, without heating surrounding plasma, knowing exactly how much power is deposited where is crucial information to the success of this method.

2.3 Electron Cyclotron Heating and Emission

The main topic of this thesis deals with the related topics of electron cyclotron heating (ECH) and electron cyclotron emission (ECE). In this section, the theory behind these concepts will be explained. While this is not necessary to understand the rest of this thesis, it may provide some theoretical background for the interested reader.

2.3.1 Electron gyromotion

The constituent particles of a fusion plasma, virtually all of them being ionized, gyrate around the magnetic field lines confining the plasma due to the Lorentz force $\vec{F}_L$:

$$\vec{F}_L = q\left(\vec{E} + \vec{v} \times \vec{B}\right), \tag{2.3}$$

with q the charge of the particle, $\vec{E}$ and $\vec{B}$ the electric and magnetic fields, respectively, and $\vec{v}$ the particle's velocity. Note that, due to the $\vec{v} \times \vec{B}$ term, the velocity of the particle pointing along the direction of the field $v_{\parallel}$ does not contribute to the force. Charged particles are therefore free to move along magnetic field lines. Any perpendicular velocity component $v_{\perp}$ causes the particles to move in circular orbits (gyrate) around the field lines. The radius of this gyration, the gyroradius ρ_g, is found by equating the Lorentz

and centripetal forces:

$$\frac{mv_\perp^2}{\rho_g} = |q|v_\perp B, \tag{2.4}$$

leading to the expression for the gyroradius in terms of the mass m of the particle, perpendicular velocity $v_\perp$ and the strength of the magnetic field B:

$$\rho_g = \frac{mv_\perp}{qB}. \tag{2.5}$$

The gyrofrequency, more commonly referred to as the cyclotron frequency ω_c, in $\mathrm{rad\,s^{-1}}$, is given by:

$$\omega_c = \frac{qB}{m}, \tag{2.6}$$

for non-relativistic particle velocities [47]. For typical magnetic field strengths in present-day tokamaks such as DIII-D, of 0.5-3 T [48], this cyclotron frequency lies in the range of 10-100 GHz.

Electrons in the high-energy tail of the velocity distribution in fusion plasmas can reach relativistic velocities, so in some cases the relativistic mass needs to be taken into account in (2.6). This is done simply by writing (2.6) as:

$$\omega_c = \frac{qB}{m_0\gamma}, \tag{2.7}$$

with m_0 the particle's rest mass, $\gamma = \frac{1}{\sqrt{1-v^2/c^2}}$, v the magnitude of the particle's velocity and c the speed of light.

Note that the direction of gyration is opposite for ions and electrons due to the charge dependence (including its sign); electrons rotate in a right-handed manner while ions rotate in a left-handed way. As can be seen in (2.6) and (2.7), the larger the magnetic field, the larger the particle charge and the smaller the particle mass, the higher the gyrofrequency. At equal magnetic fields, electrons gyrate at much higher (by m_i/m_e) frequencies than ions, tritium ions gyrate at lower frequencies than deuterium ions and doubly charged helium ions gyrate faster than tritium.

2.3.2 ECH

The gyromotion of electrons in fusion plasmas can be leveraged to change their energy in the process of Electron Cyclotron Heating (ECH). In a simplified sense, a resonance will occur between a right-handed wave oscillating at the electron cyclotron frequency and a gyrating electron, through which the electron gains energy from the wave. Intuitively, this is because the electric field component of the wave rotates at the exact frequency and in the same direction as the electron, which subsequently gets accelerated and gains energy.

In reality, this intuitive picture is not enough to describe the full situation. Since ECH is often used for localized heating, one needs to know exactly where the power will end up. This not only depends on the spatial location of the cyclotron frequency as described in (2.7) (in combination with (2.1)) but also on other plasma parameters, as well as injection geometry and the electromagnetic configuration of the injected beam.

From (2.7), a simple resonance condition is fulfilled when the frequency of the injected wave $\omega = \omega_c$. This holds when the electron's parallel velocity $v_\parallel$ is zero; taking this parallel velocity into account, the resonance condition becomes:

$$\omega = n\omega_c + k_\parallel v_\parallel, \tag{2.8}$$

with harmonic number n (i.e. not only the fundamental cyclotron frequencies but integer multiples thereof exhibit resonance) and parallel wavenumber $k_\parallel$ [49]. Note that if the electron is relativistic, ω_c depends on

the total velocity $v^2 = v_\perp^2 + v_\parallel^2$ of the electron. The second term on the right hand side of (2.8) introduces a longitudinal Doppler shift, which causes a line broadening of width

$$\Delta\omega \approx n\omega_c \frac{v_t}{c} \left| N \cos\theta \right|, \tag{2.9}$$

with v_t the thermal electron velocity (i.e. the width of the velocity distribution), N the refractive index and θ the angle of incidence of the incoming wave vector $\vec{k}$ (with magnitude $k = |\vec{k}|$) with respect to the direction of the magnetic field $\vec{B}$ $\left(\cos\theta = \frac{\vec{k}\cdot\vec{B}}{kB}\right)$. Analogously, the relativistic line broadening, due to the velocity dependence of the electron mass, is:

$$\Delta\omega \approx n\omega_c \left(\frac{v_t}{c}\right)^2. \tag{2.10}$$

From this, it can be seen that for (almost) perpendicular ECH injection $\left(|N\cos\theta| < \frac{v_t}{c}\right)$ the relativistic broadening dominates while for oblique injection (such as for ECCD), the longitudinal Doppler broadening prevails. Other line broadening mechanisms (collisional, radiative) are negligibly small [49].

In general, the relation between the (angular) frequency ω of a wave propagating through any medium and its wave vector $\vec{k}$ is nontrivial and described by a dispersion relation $\omega(\vec{k})$. The exact relation depends on the properties of the medium and for fusion plasmas; typically the cold-plasma dispersion relation is used. The solution for the refractive index N is given by the Appleton-Hartree solution, which predicts two wave modes: the ordinary (O-)mode and the extraordinary (X-)mode. They are described by:

$$\left(N^{(X,O)}\right)^2 = 1 - \frac{\omega_p^2}{\omega^2} \frac{2\left(\omega^2 - \omega_p^2\right)}{2\left(\omega^2 - \omega_p^2\right) - \omega_c^2\left(\sin^2\theta \pm \psi\right)}, \tag{2.11}$$

with

$$\psi^2 \equiv \sin^4\theta + 4\cos^2\theta \frac{\omega^2 - \omega_p^2}{\omega\omega_c}, \tag{2.12}$$

where $\omega_p = \sqrt{\frac{n_e e^2}{\epsilon_0 m_e}}$ is the plasma frequency with n_e the electron density, e the elementary charge and ϵ_0 the vacuum permittivity [50].

In this solution, the - sign in the $\pm\psi$ term denotes the O-mode, which at parallel propagation represents a left-handed circularly polarized wave while the + sign represents the right handed polarized X-mode. Since electrons exhibit right-handed gyromotion, generally the X-mode resonance will be stronger. However, it is still possible to have a resonance and apply electron heating using the left-handed O-mode. At perpendicular propagation, the O-mode is linearly polarized with its electric field component in the direction of the magnetic field and the X-mode is eliptically polarized with its electric field component perpendicular to the magnetic field.

As an example of how (2.11) is used, consider the case of perpendicular (i.e. $\theta = \pi/2$) O-mode (i.e. $-\psi$) injection. From (2.11): $\left(N^O\right)^2 = 1 - \frac{\omega_p^2}{\omega^2}$. This wave has no resonance. It does have a cut-off, however. The plasma frequency depends on the density which for a typical tokamak discharge increases from edge to center. The wave is injected at a frequency ω that exceeds ω_p at the edge of the plasma. This means that N has a real, finite value and the wave can propagate. However, as the density increases towards the center, the wave encounters a surface where its frequency equals that of the plasma frequency. The refractive index ($N \equiv ck/\omega$) goes to zero so that the wavenumber goes to zero and the wave cannot continue to propagate. Instead, it is reflected back whence it came. The X-mode does have a resonance for perpendicular injection, namely when $\omega^2 = \omega_p^2 + \omega_c^2$. At this frequency, the refractive index goes to infinity and all power is absorbed. The X-mode also has a cut-off which will not be written down here since it is a somewhat complicated and lengthy combination of ω_c and ω_p.

With these solutions to the dispersion relation, knowledge of plasma parameters (i.e. measurements of $n_e(\rho)$ to determine $\omega_p(\rho)$, measurements of $T_e(\rho)$ and $B(\rho)$ to determine $\omega_c(\rho)$) and knowledge of the geometric layout of the system (i.e. the angle θ), one can determine at what location ECH waves with frequency ω will be absorbed in the plasma. This is in fact what ray tracing codes do; by assuming a dispersion relation and analytic descriptions for the resonance condition and absorption of power the absorption location of a selection of rays (which approximates the distribution of the input beam as it exist the antenna) is calculated, based on inputs of measured profiles and a magnetic equilibrium reconstruction.

2.3.3 ECE

The resonance condition for ECH was given in (2.8). This also describes the frequency at which these gyrating electrons emit radiation in the process of electron cyclotron emission (ECE). Any charged particle emits radiation when accelerated, and any object in a circular motion is constantly accelerated; electrons in gyromotion therefore continuously emit radiation. Now, this would be a serious loss mechanism for fusion plasmas, if not for the fact that these plasmas are typically optically thick for the first and second ECE harmonics [52]. This implies that (nearly) all radiation that is emitted by the gyrating electrons is re-absorbed in the same region of the plasma such that there is a thermal equilibrium. This, in turn, means that the plasma is a black-body radiator at the first two ECE harmonics. For a black-body radiator, the intensity I of emission is related to its frequency ω and its temperature T, as described by Planck's law:

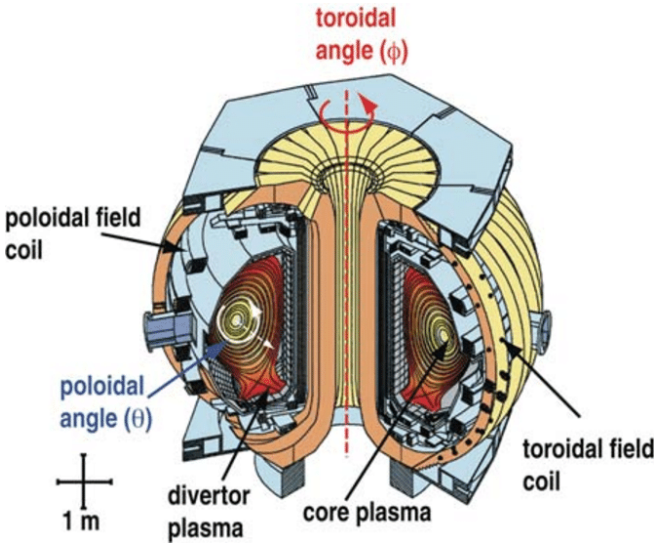

FIGURE 2.5: The DIII-D tokamak [51] is a toroidal machine, about five meters across, with a D-shaped vacuum vessel poloidal cross-section.

$$I(\omega) = \frac{\hbar\omega^3}{8\pi^3 c^2} \frac{1}{e^{\hbar\omega/T} - 1}, \tag{2.13}$$

with $\hbar = \frac{h}{2\pi}$, where h is Planck's constant. At fusion-relevant temperatures and ECH frequencies, this is very well approximated by the Rayleigh-Jeans law:

$$I(\omega) = \frac{\omega^2 T_e}{8\pi^3 c^2}, \tag{2.14}$$

with T_e the electron temperature. Therefore, by measuring the intensity of ECE radiation at a certain frequency one can directly infer the temperature from the electrons that emitted this radiation. Then, by knowing at what location in the plasma this frequency is resonant (i.e. by knowing the magnetic field as a function of space, which is something well known in tokamaks - see (2.1)), ECE can be used to make spatially resolved electron temperature measurements with a very high spatial resolution (the electron cyclotron resonance is radially very narrow, typically only millimeters) and with a very high temporal resolution (emission is continuous, so measurement is limited only by the sample frequency of the receiving device). Moreover, the technique is non-invasive.

The first harmonic (28-56 GHz for B = 1-2 T) is often shielded by the plasma frequency (typically between 30-100 GHz for n_e between 10^{19} and 10^{20} m^{-3}), so the second harmonic X-mode is usually measured [53].

A note on notation
It is customary within the nuclear fusion community to measure and write temperatures, symbol T, in units of (kilo)electronvolts. Typical temperatures encountered in fusion plasmas are on the order of $10^7 - 10^8$ K, which corresponds to average particle kinetic energies of several (tens of) keV. One electronvolt corresponds to e/k_B kelvin with elementary charge e and Boltzmann constant k_B. This same convention will be adopted throughout this thesis.

2.4 DIII-D

DIII-D (read: d-three-d) is the largest magnetic fusion device and largest tokamak in the US with a major radius of 1.7 m and a minor radius of 0.6 m, built and operated by General Atomics for the US Department of Energy [48]. DIII-D's stated mission is to "establish the scientific basis for the optimization of the tokamak approach to fusion energy production" [54]. ECH perturbation experiments related to e.g. NTM suppression and deposition profile estimation are a core part of this stated mission. DIII-D experimental data therefore provides excellent subject material for this research.

The coil configuration of DIII-D in a poloidal cross-section of the machine is shown in figure 2.4. This figure also shows the equilibrium flux surfaces (surfaces of constant temperature and density) inside the DIII-D plasma. It is these roughly D-shaped surfaces that give DIII-D the last letter in its name (with DIII short for Doublet III, the successor to the Doublet II machine) [54].

2.4.1 ECH layout

DIII-D has six gyrotrons producing 110 GHz ECH radiation [55]. Beams are co-injected at four outside dual launchers and one top launcher. This system can deliver up to 3.6 MW of ECH power for a maximum pulse duration of 5 seconds. Movable mirrors allow the injected beams to be scanned toroidally, or poloidally over an angle of 40 degrees. The beams produced by the gyrotrons have a Gaussian intensity profile[1] [56]. Figure 2.6 shows the aimings of the gyrotrons and the ECH resonance for a particular discharge (154532).

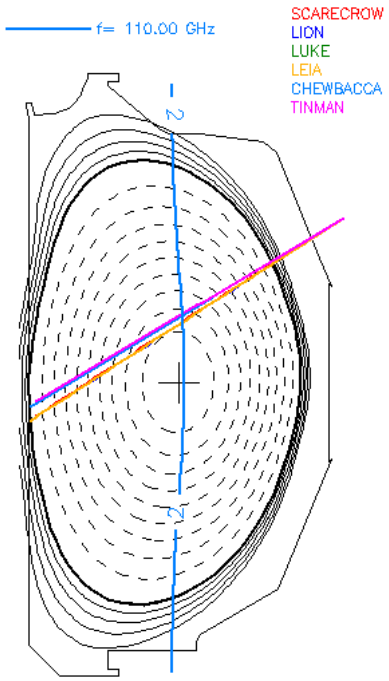

FIGURE 2.6: The ECH deposition location in DIII-D is determined by the intersection between the beam paths from the different gyrotrons (denoted by the different colors with their name in the top right) and the location of the 2nd harmonic X-mode resonance (vertical blue line), shown here for a particular DIII-D discharge 154532, plotted over the EFIT equilibrium reconstruction.

2.4.2 Diagnostics layout

An excellent overview of the more than 50 diagnostic systems installed on DIII-D can be found in [57]. The data used in this work are measured using Thomson scattering and ECE.

[1] Not related to the *deposition* profile, but the profile of the beams themselves.

Thomson scattering

A 40-channel Thomson scattering system is available for locally measuring electron temperature and densities. This is done by firing 8 pulsed Nd:YAG lasers (10 ns pulses) into the plasma, at individual rates of 20 Hz with the total system able to operate at 160 Hz continuously [58]. Bursts at rates over 10 kHz are possible for very short periods of time if the 8 lasers are fired in rapid succession, allowing for brief sampling of fast phenomena [59]. The laser photons scatter off plasma electrons in a process called Thomson scattering [60]; the number of electrons that are scattered and end up in the detector (with sight line not in the direction of the laser) is proportional to the electron density while the Doppler broadening of the wavelength of scattered light is proportional to the electron temperature. The lasers are fired along the same path through the plasma, so the 40 measurement channels are defined by the intersection between that path and the 40 lines of sight from two viewing locations (see figure 2.7).

Electron Cyclotron Emission

High time- and spatial resolution electron temperature measurements are possible in DIII-D using the Electron Cyclotron Emission (ECE) diagnostic, consisting of a heterodyne radiometer with 40 channels sampling the 83-130 GHz range of ECE radiation, each with a 1 GHz bandwidth at a rate of 100 kHz, at the plasma mid-plane [61]. The spatial resolution depends on the central magnetic field strength, the measurement location and the local electron temperature but is typically 1-3 cm (0.02 - 0.04 in normalized minor radius ρ). The system contains a notch filter at 110 GHz (the ECH frequency) to avoid potentially flooding the ECE signal with reflected ECH power.

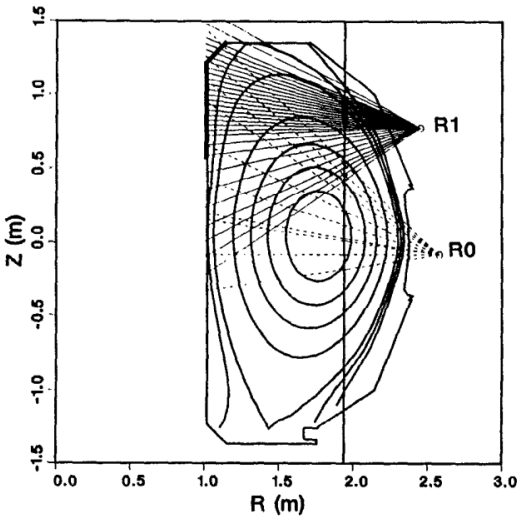

FIGURE 2.7: The measurement locations for the DIII-D Thomson Scattering system are defined by the intersection between the laser path (vertical solid line) and the lines of sight originating from two viewing points, R0 and R1, for a total of 40 measurement channels [58]. An outline of the DIII-D vacuum vessel and the flux surfaces of a typical equilibrium are shown for reference.

2.4.3 Confinement modes

The DIII-D tokamak hosts a variety of confinement modes. It contains both a limiter and a divertor, allowing for both limited and diverted L-mode plasmas as well as H-mode plasmas. The latter is characterized by an edge pressure pedestal [62] (figure 2.8).

In addition to the classic L- and H-mode plasmas, negative triangularity (L-mode) plasmas in DIII-D have been shown to exhibit H-mode-like confinement properties without the presence of ELMs [63].

Finally, the quiescent H-mode, also denoted as QH-mode, is a special case of H-mode characterized by a distinctive lack of ELMs [64] and discovered in DIII-D [65, 66], later also observed in AUG [67].

2.5 The transport equation and perturbative experiments

Perturbative experiments are a type of experiments widely used in nuclear fusion, to study transport phenomena [12, 68, 69]. In nuclear fusion, perturbative experiments refer to experiments where the parameters of a steady-state plasma (typically electron or ion temperature or density) are perturbed by some source (of heat, particles, ...). In this thesis, perturbative experiments refer in particular to experiments where an ECH source is modulated, i.e. varied in strength over time, such that the electron

temperature fluctuates periodically around a steady-state value. Measuring these temperature fluctuations allows the spatial deposition profile of the perturbing source to be estimated, as will be explained in subsequent sections.

To understand how the measurement of electron temperature fluctuations relate to the spatial profile of the source, the electron energy transport equation is used. Generally, it is written as [12]:

$$\frac{3}{2}\frac{\partial}{\partial t}\left(n_e T_e\right) = -\nabla\cdot\left(\boldsymbol{q}_e + \frac{5}{2}T_e\boldsymbol{\Gamma}_e\right) + \boldsymbol{\Gamma}_e\cdot\frac{\nabla\left(n_e T_e\right)}{n_e} + S, \tag{2.15}$$

with density n_e, temperature T_e, heat flux $\boldsymbol{q}_e$, particle flux $\boldsymbol{\Gamma}_e$, source S and the subscript e for electron. The source term S contains all heat sources and sinks. In principle, all quantities in (2.15) are both space- and time dependent, so the explicit dependencies are left out for the sake of brevity. A diffusive-convective model is assumed for the heat flux that depends on the diffusivity D and convective velocity U in the following way:

$$\boldsymbol{q}_e = -n_e D\nabla T_e - n_e U T_e. \tag{2.16}$$

Plugging (2.16) into (2.15), assuming one-dimensional cylindrical geometry (so that $\nabla f = \frac{\partial f}{\partial\rho}$ and $\nabla\cdot\boldsymbol{A} = \frac{1}{\rho}\frac{\partial}{\partial\rho}\left(\rho\boldsymbol{A}\right)$, with (2.2) defining ρ), and with some re-writing, one arrives at the following [28]:

$$\frac{3}{2}\frac{\partial}{\partial t}\left(n_e T_e\right) = \frac{1}{\rho}\frac{\partial}{\partial\rho}\left(\rho n_e D\frac{\partial T_e}{\partial\rho} + \rho n_e V T_e\right) + n_e K T_e + S, \tag{2.17}$$

where convectivity $V = U + \frac{7}{2}\frac{\Gamma_e}{n_e}$, reactivity (sometimes referred to as damping) $K = \frac{1}{n_e}\left(\frac{\partial\Gamma_e}{\partial\rho} - \frac{1}{n_e}\frac{\partial n_e}{\partial\rho}\Gamma_e\right)$, where Γ_e is a scalar denoting the magnitude of the particle flux $\boldsymbol{\Gamma}_e$ and where its sign denotes the direction (positive for towards increasing ρ and negative for towards decreasing ρ). The source term S contains all sources and sinks of heat that keep the plasma in steady state, as well as the modulated ECH source S_{MECH}: $S = S_{in} - S_{out} + S_{MECH}$. The modulated ECH source S_{MECH} consists of a spatial power deposition profile $P(\rho)$ and a modulation in time $\tilde{U}(t)$: $S_{MECH} = P(\rho)\tilde{U}(t)$. This modulation $\tilde{U}$ causes a perturbation of the electron temperature T_e, such that $T_e = T_0 + \tilde{T}_e$ where T_0 is the steady-state temperature and $\tilde{T}_e$ represents the temperature perturbation around T_0.
Two big assumptions are made (which are often made in literature, e.g. [12, 27, 28]), namely that the density n_e is not perturbed by the modulated ECH source such that $\tilde{n}_e = 0$, and that the perturbation is sufficiently small such that $\tilde{T}_e$ is only a first-order term and the thus the response may be assumed to be linear[2]. The validation of these assumptions is discussed in section 5.2. These two assumptions allows writing (2.17) only in terms of the temperature perturbation $\tilde{T}_e$, the modulated source $P(\rho)\tilde{U}(t)$ and the steady-state density n_e:

$$\frac{3}{2}n_e\frac{\partial\tilde{T}_e}{\partial t} = \frac{1}{\rho}\frac{\partial}{\partial\rho}\left(\rho n_e D\frac{\partial\tilde{T}_e}{\partial\rho} + \rho n_e V\tilde{T}_e\right) + n_e K\tilde{T}_e + P\tilde{U}, \tag{2.18}$$

where all quantities except $\tilde{U}$ depend on ρ and only the quantities with a tilde depend on time. The spatial power deposition profile $P(\rho)$ can be estimated using (2.18) based on measurements of $n_e(\rho)$ and $\tilde{T}_e(\rho,t)$. The same holds for the other spatially dependent parameters D, V, K. This can be done in different ways, five of which are discussed in the following sections and applied in subsequent chapters of this thesis. Note that in the nuclear fusion literature, a distinction is made between perturbative or heat pulse transport parameter estimates and so-called 'power balance' estimates, obtained by assuming

[2]Linearity in the sense that it follows the superposition principle: increase the power by a factor x and the temperature perturbation amplitude will be x times larger; add a second perturbing source and the temperature perturbation will be the sum of the responses to each source individually.

steady state (i.e. setting the left-hand side of (2.18) to zero) [12, 70]. In (2.18) and in this thesis, we consider only the former.

2.6 Deposition profile estimation methods

As stated in the previous section, (2.18) can be used to estimate the ECH deposition profile $P(\rho)$. There are different ways to solve (2.18) for $P(\rho)$, using different approaches to e.g. boundary conditions, leading to different estimation methods. The five methods that are applied to DIII-D measurement data to obtain the results in this thesis are described in this section.

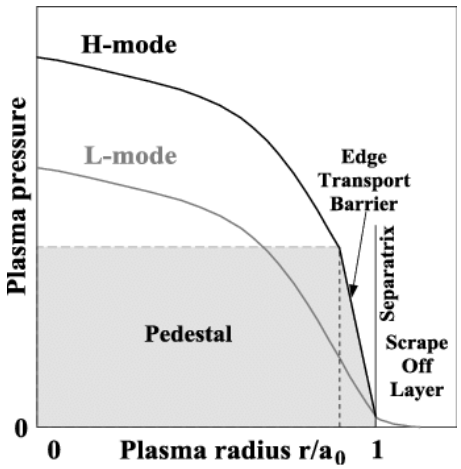

FIGURE 2.8: The H-mode plasma pressure profile shows a characteristic pedestal near the plasma edge, that forms a transport barrier, leading to much better performance than L-mode plasmas without such a barrier [71].

2.6.1 Break-in-slope

To use the break-in-slope method [22, 72], the source modulation $\tilde{U}(t)$ should be a step or a square wave. That is, there should be a change in power level applied to the plasma on a time scale τ_P much faster than the characteristic diffusive or convective timescales. From experience, the DIII-D ECH source can switch on a time scale $\tau_P = \mathcal{O}\left(10^{-4}\right)$ seconds. The diffusive time scale $\tau_D \propto a^2/D = \mathcal{O}\left(0.5\right)$ s, for $a = 0.67$ m (DIII-D) and a typical value of $D \approx 1$ m^2/s, dominates transport [34]. For time scales shorter than τ_D, then, the fast change in power level must be directly reflected in a discontinuous (compared to τ_D) slope of the temperature signal $\frac{\partial \tilde{T}_e}{\partial t}$, i.e. a break in the slope. The difference in power that was deposited during the step can be determined from difference in slope of the temperature the instant before (t_-) and the instant after (t_+) the step in power:

$$\begin{aligned} P(\rho) &= P_{MECH}(\rho, t = t_+) - P_{MECH}(\rho, t = t_-) \\ &= \frac{3}{2} n_e(\rho) \left(\frac{\partial \tilde{T}_e}{\partial t}(\rho, t = t_+) - \frac{\partial \tilde{T}_e}{\partial t}(\rho, t = t_-) \right), \end{aligned} \tag{2.19}$$

again, assuming $\nabla \cdot \tilde{\boldsymbol{q}}_e(\rho, t = t_+) - \nabla \cdot \tilde{\boldsymbol{q}}_e(\rho, t = t_-) = 0$. Note that this method fails in the presence of highly elevated transport (e.g. high diffusion and/or significant convection) or when the source cannot switch power level fast enough, such that $\tau_P \gg \tau_{D,V}$ does not hold.

The break-in-slope method requires the evaluation of the slope of the temperature signal $\frac{\partial \tilde{T}_e}{\partial t}$ on the timescale of τ_P which, in practice, is difficult due to the presence of noise. Therefore, a function is fit to the $\tilde{T}_e$ signal before and after the break in slope, from which an analytic derivative can be calculated and evaluated at t_- or t_+.

2.6.2 Fast Fourier transform

The Fast Fourier Transform (FFT) method circumvents the issue of having to determine time derivatives by transforming the time domain signal to the frequency domain through a discrete Fourier transform (DFT) of a time-domain signal [73]. Note that, while the FFT algorithm is a specific implementation of the Fourier transform, the use of the FFT to compute discrete Fourier transforms has become so widespread that the FFT has practically become synonymous with the discrete Fourier transform in general. In literature one speaks generally of the FFT method rather than simply the Fourier transform

or FT method, e.g. [72]. In accordance to literature, this method will therefore be called the FFT method rather than the FT method.

The Fourier transform is a unitary operator (Parseval's theorem), such that the FT of (2.18) may be taken without loss of information, and reads:

$$\frac{3}{2}n_e i\omega\tilde{\Theta} = \frac{1}{\rho}\frac{\partial}{\partial\rho}\left(\rho n_e D\frac{\partial\tilde{\Theta}}{\partial\rho} + \rho n_e V\tilde{\Theta}\right) + n_e K\tilde{\Theta} + P\tilde{\Upsilon}, \tag{2.20}$$

where $\tilde{\Theta}(\omega,\rho) = \mathcal{F}\{\tilde{T}(\rho,t)\}$ and $\tilde{\Upsilon}(\omega) = \mathcal{F}\{\tilde{U}(t)\}$, with $\mathcal{F}\{\}$ the Fourier transform. By simply assuming the transport terms (related to D, V, K) are negligible compared to the power deposition term P, $P(\rho)$ can be directly computed from (2.20):

$$P(\rho) = \frac{3}{2}n_e i\omega\frac{\tilde{\Theta}(\rho,\omega)}{\tilde{\Upsilon}(\omega)}. \tag{2.21}$$

Note that this assumption holds true when $\omega \to \infty$ [28, 29]. Whether or not it this assumption holds for the analysis of DIII-D data is discussed in section 4.1.1.
Note also that while (2.20) is defined based on the continuous Fourier transform, in reality only the discrete FFT is used to transform the measured $\tilde{T}(\rho,t_k)$ signal to $\tilde{\Theta}(\omega_k,\rho)$ at discrete frequency bins $\omega_k \leq 2\pi F_N$ with F_N the Nyquist frequency. Implicitly it is assumed that an anti-aliasing filter is applied in a pre-processing step to generate the measured data $\tilde{T}(\rho,t_k)$, which is almost always the case. With this in mind, for the sake of simplicity of notation we stick to the continuous Fourier transform derivation of (2.20) (and subsequent frequency-domain equations).

2.6.3 Maximum likelihood estimator

The sample maximum likelihood estimator (MLE) is, as the name suggests, a method to estimate the parameters D, V, K, P in (2.20) by maximizing the likelihood function between (2.20) with estimated parameters $\hat{D}, \hat{V}, \hat{K}$ and $\hat{P}$ and the set of measured $\tilde{\Theta}(\rho,\omega)$ [28, 29, 31]. Maximizing the likelihood function is analogous to finding $\hat{D}, \hat{V}, \hat{K}$ and $\hat{P}$ that maximize the probability of 'drawing' the measured $\tilde{\Theta}(\rho,\omega)$ from a random population according to some probability function [74].

The MLE as used in this thesis assumes that parameters D, V, K and P are constant on three-point sub-domains, where the most likely parameter values are estimated for the center measurement point in these three-point domains based on an estimate of the uncertainty in the temperature measurements. By sliding the three-point window over the entire measurement domain and estimating the parameters D, V, K and P separately for each central point, spatially varying profiles can be estimated in a point-wise manner. The MLE improves over the break-in-slope and FFT methods in that it can estimate transport parameters and power deposition simultaneously, does not rely on fitting functions to determine the slope and that it takes some measure of uncertainty into account. Below, a more detailed overview of the method is given.

Like the FFT method, the MLE uses (2.20) rather than (2.18) since it circumvents the issue of time derivatives. Moreover, (2.20) is a partial differential equation (PDE), which are notoriously difficult to solve. Rather, (2.20) is a complex-valued ordinary differential equation (ODE), for which solutions can be more easily computed. The ODE in (2.20) is independent for each frequency ω and requires boundary conditions to solve, which are highly context dependent and therefore not known in general. The MLE as implemented in this thesis solves this issue using the three-point sub-domain: given that there are N spatial measurement points, i.e. sensor locations, the MLE solves (2.20) for each spatial measurement point $\rho_i \in [\rho_{1+n},...,\rho_{N-n}]$ where the temperature measurements $\tilde{\Theta}(\rho_{i-n},\omega)$ and $\tilde{\Theta}(\rho_{i+n},\omega)$ are used as boundary conditions (figure 2.9).

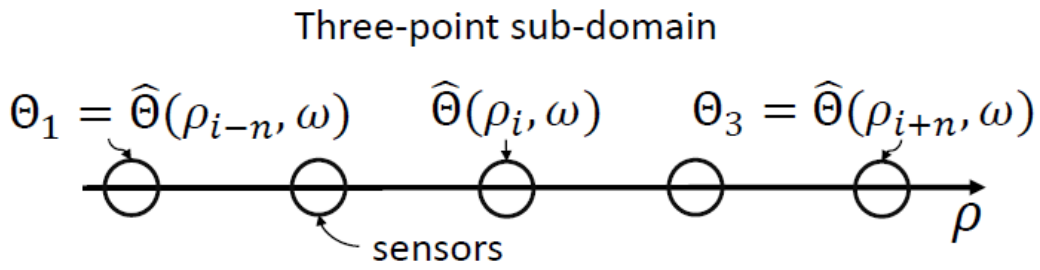

FIGURE 2.9: A three-point subdomain, consisting of Fourier transformed temperature measurements at three spatial locations, can be used to solve a one-dimensional differential equation on a spatial grid (line), by using the extremum measurements $\Theta(\rho_{i+n})$ as boundary conditions to solve for the parameters of interest in the middle point.

Using this, the transfer functions from $\tilde{\Theta}(\rho_{i\pm n}, \omega)$ to $\tilde{\Theta}(\rho_i, \omega)$ are (numerically) computed, from which the likelihood function can be constructed for the parameters D, V, K and P. See [28] or [29] for the exact definitions of the transfer- and likelihood functions. Again, maximum of the likelihood function represents the set of D, V, K, P that is most likely to explain the measurements $\tilde{\Theta}(\rho, \omega)$, given the uncertainty in those measurements. The MLE therefore requires an estimate of that uncertainty, which is given by the covariance $\sigma^2(\omega, \rho_i, \rho_j)$ between temperature measurements at sensor locations ρ_i and ρ_j at a given frequency ω. This covariance can be computed by comparing the Fourier coefficients from the Fourier transform of each individual period in the temperature signal to the average over all periods, and is given by:

$$\hat{\sigma}^2_{j,i}(\omega, \rho_j, \rho_i) = \frac{1}{M(M-1)} \sum_{m=1}^{M} \left(\tilde{\Theta}^{[m]}(\omega, \rho_j) - \hat{\Theta}(\omega, \rho_j) \right) \overline{\left(\tilde{\Theta}^{[m]}(\omega, \rho_i) - \hat{\Theta}(\omega, \rho_i) \right)}, \tag{2.22}$$

where M is the number of periods in the signal, $\tilde{\Theta}^{[m]}(\omega, \rho_j)$ is the Fourier coefficient of period m at frequency ω and sensor location ρ_j, $\hat{\Theta}(\omega, \rho_j)$ is the mean of Fourier coefficients from all M periods at frequency ω and sensor location ρ_j, and the overbar denotes the complex conjugate. In this way, the MLE takes into account the measurement uncertainty on the temperature based on the variation between periods. The likelihood function is currently optimized using a gradient-based interative solver.

2.6.4 Frequency domain least squares estimator

The Frequency Domain Least Squares estimator (abbreviated FDLS) [32], like the MLE, estimates the parameters D, V, K and P in (2.20), i.e. in the frequency domain. In contrast to the MLE, however, there is no assumption of locally constant parameters; rather spatially varying parameters $D(\rho), V(\rho), K(\rho)$ and $P(\rho)$ are estimated by fitting continuous functions. In addition, the spatially varying density $n_e(\rho)$ and its gradient is taken into account. This has the advantage over the MLE of being less sensitive to local signal-to-noise ratios (SNRs) but comes at the cost of potential spatial aliasing.

Like the MLE method, the FDLS method solves (2.20). Including all spatial and frequency dependencies, it reads:

$$\frac{3}{2} n_e(\rho) i\omega \tilde{\Theta}(\rho, \omega) = \frac{1}{\rho} \frac{\partial}{\partial \rho} \left(\rho D(\rho) n_e(\rho) \frac{\partial \tilde{\Theta}}{\partial \rho}(\rho, \omega) - \rho V(\rho) n_e(\rho) \tilde{\Theta}(\rho, \omega) \right) + n_e(\rho) K(\rho) \tilde{\Theta}(\rho, \omega) + P(\rho) \tilde{\Upsilon}(\omega). \tag{2.23}$$

The boundary conditions for this equation are, similar to the MLE method, given by measurement points. Since the FDLS method fits functions through the entire domain, the outer two points of the domain ρ_1 and ρ_N are taken as boundary conditions.

To solve (2.23), the unknown $\gamma = \mathrm{col}\,(D(\rho), V(\rho), K(\rho), P(\rho))$ are written as a sum of R basis functions $B_r(\rho) = \mathrm{diag}\left(B_r^D(\rho), B_r^V(\rho), B_r^K(\rho), B_r^P(\rho)\right)$ which are linear in their coefficients θ:

$$\gamma(\rho, \theta) = \sum_{r=1}^{R} B_r(\rho)\theta_r, \tag{2.24}$$

with $B_r^X(\rho)$ the r^{th} basis function describing parameter X as a function of ρ. These basis functions can be e.g. polynomials of order $R-1$ and θ_r the corresponding coefficients, so that $\sum_{r=1}^{R} B_r(\rho) = 1 + \rho + \rho^2 + ... + \rho^{R-1}$ and $\theta_r = \mathrm{col}\left(\theta_r^D, \theta_r^V, \theta_r^K, \theta_r^P\right)$ contain the coefficients for ρ^{r-1} term. However, these basis functions need not be polynomials but can be B-splines, Fourier series coefficients or any other basis functions, as long as they have well defined first and second derivatives. In this way, the problem reduces to estimating the coefficients $\theta = \mathrm{col}\,(\theta_1, ..., \theta_R)$, from which γ can be computed.

After the parametrization of the parameters, (2.23) is discretized using a central finite difference scheme for the spatial derivatives and by considering a specific (excited) frequency ω_k and cast into state-space form:

$$\begin{aligned} i\omega_k \boldsymbol{\Theta}(\omega_k) &= A(\theta)\boldsymbol{\Theta}(\omega_k) + B(\theta)\boldsymbol{\Upsilon}(\omega_k) \\ Y(\omega_k) &= C\boldsymbol{\Theta}(\omega_k), \end{aligned} \tag{2.25}$$

with the state vector $\boldsymbol{\Theta}(k) = \mathrm{col}\,(\Theta(\rho_2, \omega_k), ..., \Theta(\rho_{N-1}, \omega_k))$ and the extended input vector $\boldsymbol{\Upsilon}(\omega_k) = \mathrm{col}\left(\tilde{\Upsilon}(\omega_k), Y(\rho_1, \omega_k), Y(\rho_N, \omega_k)\right)$. $A(\theta)$ and $B(\theta)$ contain the coefficients to be estimated; they are linear in those coefficients and they result from the finite difference scheme and the boundary conditions. See [32] for a detailed description of their structure. The matrix C maps the states to the outputs. To find the optimal solution for the coefficients in θ, the equation error is defined:

$$\nu_{ee}(\theta) = \sum_k \left|\left| i\omega_k \tilde{\Theta}_k - \left(A(\theta)\tilde{\Theta}_k + B(\theta)\Upsilon(\omega_k)\right)\right|\right|^2, \tag{2.26}$$

which is a least-squares estimation problem that is fully linear in the coefficients θ. This has the following closed-form solution [32]:

$$\hat{\theta} = \left(\left(\bar{A} + \bar{B}\right)^{\mathrm{H}} \left(\bar{A} + \bar{B}\right)\right)^{-1} \left(\bar{A} + \bar{B}\right)^{\mathrm{H}} \bar{\Upsilon}, \tag{2.27}$$

with Hermitian transpose $^{\mathrm{H}}$ and the column concatenations $\hat{A}\left(\hat{\Theta}(\omega_k)\right)$, $\hat{B}\left(\hat{\Theta}(\omega_k)\right)$ and $i\omega_k\hat{\Theta}(\omega_k)$ denoted by $\bar{A}$, $\bar{B}$ and $\bar{Y}$, respectively. This closed-form solution is unique and extremely rapidly computable since it requires no iteration or optimization to solve, merely direct evaluation.

2.6.5 Flux fit

This method is an adaptation of the method used by Brookman et al., described in [27]. The original method relies on a strictly Gaussian parametrization of the source profile $P(\rho)$ with a single degree of freedom (the Gaussian width). For this work, the number of parameters in $P(\rho)$ is extended from one to four, including a shift, scale and skew parameter to provide the necessary freedom to more accurately be able to estimate $P(\rho)$. At the time of writing this thesis, publication is being written on this extension to the method in [27]. This publication is contained, verbatim, in section 3.3.

Units of D and V estimations
All parameter estimations described in this section concern estimation of spatial profiles involving spatial derivatives over a *normalized* spatial coordinate ρ, which is, by virtue of being normalized, dimensionless. This implies that estimations of diffusion D and convection V are estimated in units of s^{-1}. To convert these to physical units of m^2/s and m/s, D and V are multiplied by a^2 and a, respectively, with a the plasma minor radius in m. This can be verified by substituting $r \approx a\rho$, with r and a both in m into e.g. (2.20).

2.6.6 Ray tracing methods

Several types of codes exist to numerically compute propagation and absorption of waves through fusion plasmas based on theoretical models, broadly separated into four categories: full-wave, ray-tracing, Gaussian beam and quasi-optical codes [75]. Full wave simulations are computationally expensive and are therefore mostly substituted with one of the latter three. Ray tracing codes, e.g. TORAY, start by assuming a narrow Gaussian power distribution of the input beam. They select a small number of rays, typically 30-100, to describe this distribution. Each of these rays is subsequently propagated individually without interaction and absorption is calculated for each ray separately. This may lead to deposition profiles different than the initial beam profile. Since there is no interaction between the rays, ray tracing codes do not take wave-optical effects such as diffraction and interference into account.

Gaussian beam codes (e.g. TORBEAM) do take such wave-optical effects into account by propagating a beam with Gaussian intensity profile and maintaining this profile along propagation. Imagine, for instance, a focused beam. In a ray tracing simulation, rays may cross each other in a single point, while a Gaussian beam code would maintain a finite waist size. This is an improvement over ray tracing codes in situations where diffraction and/or interference are significant, but misses freedom in determining the deposition profile which may cause this type of code to miss important deposition physics. Deposition is calculated by assuming all the power is in the central 'ray' of the beam. Whenever some fraction of that central power is absorbed, that deposited power is spread over the cross-section of the beam. This means that absorption away from the beam center is not calculated, it is assumed the beam stays Gaussian in profile. This discrepancy is especially important in beams with large divergence or injection at oblique angles (when the beam approaches the resonance from a small angle), so in these cases it might be better not to deploy a Gaussian beam code.

Finally, quasi-optical codes (e.g. GRAY) work similarly to ray-tracing codes, with the inclusion of interactions between the rays. Quasi-optical codes are therefore able to take wave behavior (diffraction and interference) into account without forcing the profile of the beam.

All codes use a dispersion relation to calculate propagation of the beam and some resonance and absorption model. The dispersion relations used are typically the cold plasma or sometimes the relativistic dispersion relation. Resonance is usually weakly or fully relativistic, and absorption is modeled through various descriptions including Fokker-Planck and (weakly) relativistic ones. The choice of dispersion relation and absorption models is independent of the type of beam code used and can vary between versions of the same code (e.g. TORAY-FOM and TORAY-GA use different absorption models) [75]. The version used in this thesis is TORAY-GA[75], with a weakly relativistic absorption mode, which will sometimes be denoted simply as TORAY.

Chapter 3

Data processing and estimation method implementation

The work in this thesis encompasses analyzing experimental data, which makes data processing a crucial part of the process. This chapter will discuss the approach that is taken to process the experimental data. Moreover, only two out of five power deposition estimation methods have readily available numerical implementations: the Maximum Likelihood Estimator (MLE) and the Frequency Domain Least Squares estimator (FDLS). The other three, the break-in-slope (BIS), fast Fourier transform (FFT) and flux fit (FF) methods, are implemented separately. The FFT method is a implemented directly based on (2.21), but the implementation of the remaining two methods (BIS and FF) are discussed in this chapter after the data processing.

3.1 Data processing

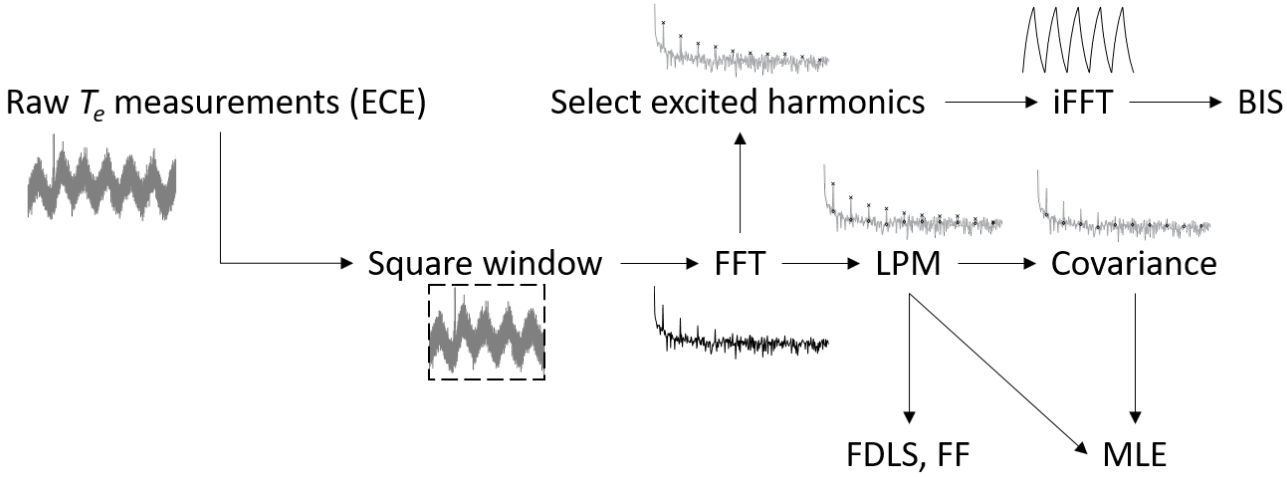

FIGURE 3.1: Data in this thesis is processing in the following way, as indicated by this flowchart: raw electron temperature measurements are windowed, transformed to the Fourier domain, then either the excited harmonics are selected and transformed back to the time domain before being analyzed using the BIS method (section 2.6.1), or the LPM is applied. After the LPM either the FDLS and/or FF methods can be applied directly, or using the covariance estimate from the LPM the MLE mehtod is used.

The data processing for this work consists of a number of steps, shown schematically in figure 3.1. The raw ECE measurements are windowed such that the signal is cut to an integer number of periods. This is important for the Fourier transform, which is the next step, and will be explained in more detail in section 3.1.1. For the break-in-slope method all non-excited frequency components are removed before

inverse transforming the spectrum back to the time domain, such that the resulting signal contains only the harmonic content directly originating from the perturbative source. For the other methods, the local polynomial method (LPM, section 3.1.3) is applied to remove any trends in the signal that persist at the excited frequencies. From here, either the FDLS and/or FF estimation methods are directly applied, or the covariance estimate from the LPM output is combined with spectral information from the LPM such that the MLE can be applied.

3.1.1 Fourier transform

The majority of the work in this thesis relies on analyzing time-series measurements in the frequency domain. A well implemented DFT is therefore essential, which refers in particular to minimizing spectral leakage, an effect whereby excited frequencies in the spectrum do not neatly fall into the frequency bins set by the DFT algorithm and therefore are spread out over neighboring frequency bins [76]. This effect is minimized by truncating the periodic signal to an integer number of periods. In the ideal case, the fundamental frequency of the signal f_0 and the sample frequency F_s are chosen such that the number of samples in one period $N_s = F_s/f_0$ is an integer. In this case, the signal can be truncated at any integer multiple of N_s samples and no spectral leakage will occur. In the next best case, N_s is not an integer but there exists a number of periods N_p such that $N_p \cdot N_s$ is an integer and is less than the total number of samples in the signal. The effect of spectral leakage will be minimized in this case. In all other cases, the signal should be truncated at a number of periods N_p such that $N_p \cdot N_s$ is as close to an integer as possible. Figure 3.2b shows a case where the signal is truncated at $N_p \cdot N_s$ samples with $N_p \cdot N_s$ an integer number of samples and $N_p > 1$. In contrast, figure 3.2a shows the spectrum of a periodic signal that was not truncated at an integer number of periods. This extra fraction of a period in the DFT increases artifacts in the spectrum that are not actually present in the signal and causes a shift in the frequency bins. As a result, the spectrum is distorted and the estimated excited frequencies, denoted by the orange crosses, are not at the amplitudes they are expected to be.

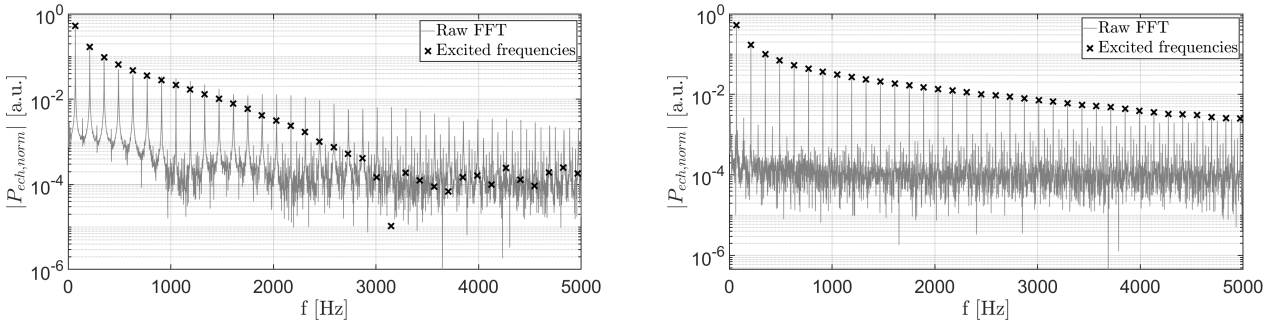

(A) (B)

FIGURE 3.2: The importance of correctly truncating a periodic signal when computing a Discrete Fourier Transform (DFT) spectrum, as showcased by the distortion of the spectrum (A) due to spectral leakage on the left when leaving a fraction of a period in the signal before applying the DFT. In (B), the spectrum is truncated at an integer number of periods such that its inherent shape is resolved.

3.1.2 FFT filtering for BIS

The break-in-slope method requires fitting noisy time domain signals, so the optimal implementation includes noise filtering. For this work, a Fourier transform-based noise filter was implemented, to simultaneously reduce noise, correct for transients and to recover the intrinsic signal shape. The modulated ECH waveform and thereby its harmonic content is very well known. For a square wave, for instance, like that in figure 3.3, only the odd harmonics of the fundamental (modulation) frequency (50 Hz in the figure) contribute to the signal. Only these frequencies should therefore contribute to the temperature

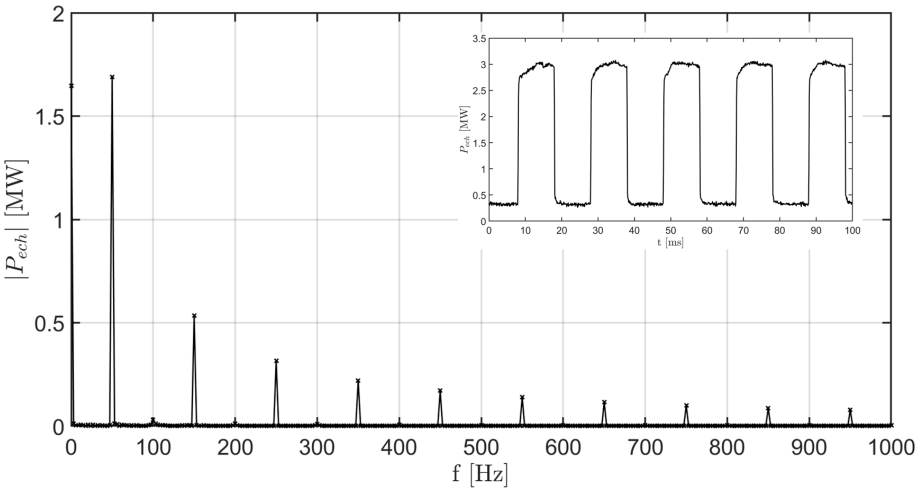

FIGURE 3.3: Fourier spectrum of a 3 MW ECH source modulated between 10 and 100 % power at 50 Hz with an approximately square waveform.

signals resulting directly from the source modulation and all other frequencies present in the temperature signals are either noise or from other sources unrelated to the modulated source perturbation.

Based on this principle, a great way to filter signals resulting from a source with known harmonic components is to numerically Fourier transform the time-domain signals, e.g. using an FFT algorithm, setting all of the resulting Fourier coefficients not corresponding to the frequencies present in the source to zero, and inverse transforming the resulting signal back to the time domain. An illustrative example of this filter, applied to a T_e time trace from DIII-D discharge 165078 is shown in figure 3.4. The filtered signal (in black) is virtually noise-free, contains no trends or other fluctuations, and clearly shows the intrinsic signal shape resulting from the modulated source. Note that the FFT is taken over the entire time trace, so that all periods in the filtered signal are exactly the same since the FFT taken over multiple periods averages the coefficients over those periods. This has the added benefit that the break-in-slope procedure only has to be applied once, to an arbitrary period in the signal, since any other period will yield the exact same result.

This filter, henceforth referred to as the FFT filter, is implemented for the break-in-slope method used in this work.

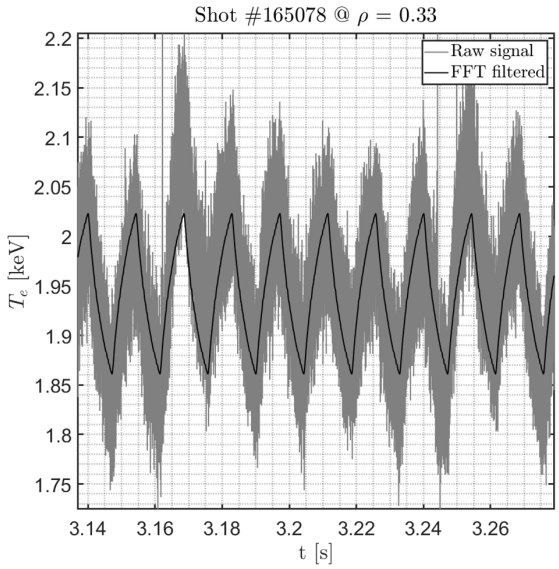

FIGURE 3.4: Applying an FFT filter (i.e. Fourier transforming a periodic time-domain signal resulting from a periodic source, removing any frequencies not present in the source and inverse Fourier transforming back to the time domain) to a raw ECE electron temperature measurement (in gray) yields the filtered signal in black, with significant noise and trend reduction.

3.1.3 Transient removal using the Local Polynomial Method

Transients due to initial conditions or drift effects influence estimation results by burying underlying processes and therefore need to be filtered. This can be done both in time and in frequency domain.

Typically, transients are filtered in the time domain by fitting and subtracting high (5th or 6th) order polynomials to the data (e.g. [27]). This ensures that the most significant baseline trends are removed. A more reliable and robust method that can be used for frequency domain estimation techniques is the Local Polynomial Method (LPM) [77, 78]. This method assumes that drifts and transients in time domain behave like smooth (polynomial) functions in frequency domain, particularly at low frequencies. Using this assumption, it fits low (usually 2nd) order polynomials to the Fourier coefficients in the complex plane. The fit is made very locally, so that the fit order does not need to be very high. In this way, frequency components that are expected to be visible in the spectrum (multiples of the modulation frequency/frequencies) but are obscured by transients at low frequencies can be recovered. Using the fit residuals, the (co)variance of the measurements in can be estimated [79], which can thereafter be used in e.g. the MLE method. Figure 3.5 shows the improved accuracy of the LPM over traditional time-domain fitting methods.

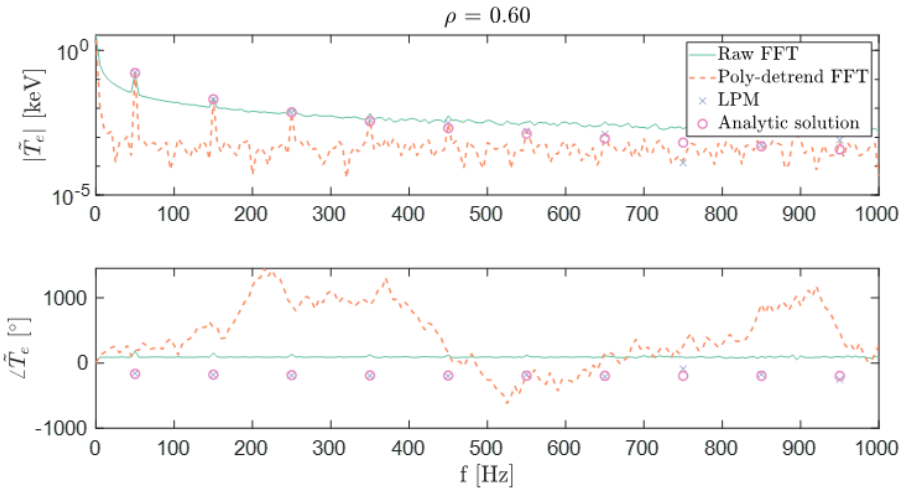

FIGURE 3.5: A traditional method of time-domain polynomial detrending (orange dashes) performs well in resolving the analytic solution (pink circles) in the amplitude spectrum of a simulated spectrum that contains a large trend (green line) burying most of the excited frequencies, but it introduces time delays which manifest themselves in the phase spectrum. The Local Polynomial Method [77, 78] (blue crosses) accurately resolves the analytic solution from the spectrum with trend in both the amplitude and phase parts of the spectrum, up to the 7th harmonic in this particular case.

3.2 Break-in-slope implementation

The details of the break-in-slope method are described in section 2.6.1; the method fits a function to a temperature signal just before and just after a "break-point" in the signal, caused by the (near) instant turn-on or turn-off of the source. The slope of the temperature at the instants before and after the break-point is determined from the fits and compared to find the amount of power deposited. Accurate and robust implementation of this method requires accurate and robust determination of (the slope of) the fit function, which typically requires extensive noise filtering on the signal to recover its intrinsic characteristic shape, and the break-points, which in turn also requires noise removal. Noise removal was discussed in section 3.1.2, so this section will focus on break-point detection and function fitting.

3.2.1 Break-point detection

Typically, the instants in time where the source-induced break-points in the temperature signals occur for each position in the plasma are simply assumed to correspond exactly to the time instances where the source is instantaneously modulated in power level. However, this is not necessarily a good assumption. There may be (non-)physical time differences between the ECH signal and the measured temperature signals due to poor time calibration, fast transport that quickly redistributes power radially or in the case of minority heating such as measuring the electron response to ion cyclotron heating (or vice versa) [72]. A more robust break-in-slope routine therefore detects the break-points in each temperature signal rather than rely on the source signal switching instances. For this work, a break-point detection algorithm was developed and implemented based on the most statistically significant change in the slope of the signal. Figure 3.6 shows an illustrative example.

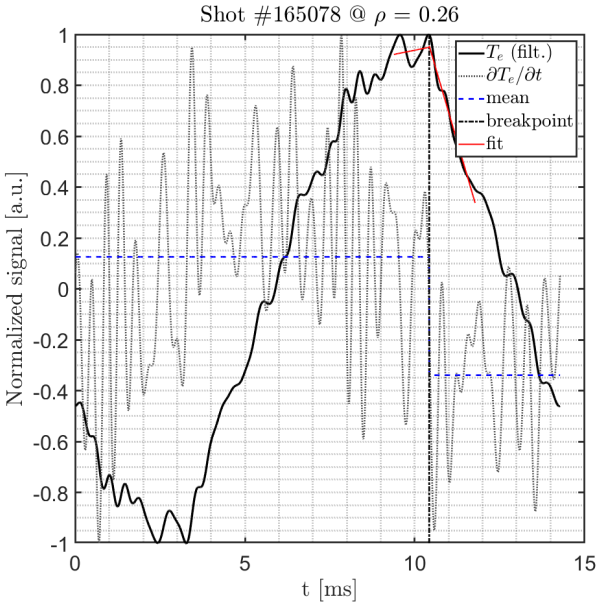

FIGURE 3.6: Break-point detection of a periodic temperature signal (in black) is done based on finding the location where the mean (shown in blue dash-dot) of the signal slope (calculated using finite difference, shown in gray dashes) varies most significantly between both sides of the break point (vertical line). Based on this break-point, linear fits of the signal (shown in red) can be made on both sides to determine the difference in slope of the signal between before and after the break-point.

In the figure, a single period of an FFT filtered temperature signal is shown in black. The slope (in gray dashes) is determined using a finite central difference scheme. The signal is split in two, and the mean of each side (shown in blue dashes) of the signal is determined. The location of the divide is then moved along the signal, and the location where the mean on both sides of the split is most significant is determined to be the break-point (indicated with the vertical dash-dotted line). This method circumvents problems with simple peak detection, as evident from this example, where the peak left of the peak associated with the detected break-point would have been selected, or determining where the derivative of the signal goes through zero, which happens in multiple locations besides the correct break-point due to imperfect filtering.

3.2.2 Fit function

In section 2.6.1 it is mentioned that a function is fit to the temperature signal in order to evaluate the slope at the break point. In this work, a simple linear fit is chosen due to its ease of implementation and relative robustness to fluctuations that remain in the signal, such as can be seen in figure 3.6. Sometimes in other works (e.g. [22]) exponential fits are implemented, but often these are fit by hand on a case by case basis. In this work, the fitting procedure is automated to be able to quickly, flexibly and reliably analyze large amounts of data. For multi-parameter, nonlinear fits such as the exponential fit in [22], this requires iterative optimization which strict upper and lower bounds on the fit parameters which vary on a case-by-case basis, to avoid bad fits due to local minima in the cost function. In practice, therefore, the simple linear fit has proven the most reliable and robust method in this work.

3.3 Flux fit implementation

As stated at the beginning of chapter 3, the remainder of this chapter contains, verbatim, the contents of a publication (in the making at the time of writing this thesis) on the extensions that are made to the method as described in [27] for estimating ECH deposition profiles based on perturbative electron temperature measurements. Symbols and conventions may therefore deviate from those in other sections of this thesis. Note that the publication is still a work in progress; the final published version may differ from the version included here.

Extension of the flux fit method for estimating power deposition and heat transport

J.H. Slief,[1,2] M. van Berkel,[1] M.W. Brookman,[3] and R.J.R. van Kampen[1,4]
[1)]*DIFFER - Dutch Institute for Fundamental Energy Research, De Zaale 20, 5612 AJ Eindhoven, the Netherlands*
[2)]*Science and Technology of Nuclear Fusion, Department of Applied Physics, Eindhoven University of Technology, P.O. Box 513, 5600 MB Eindhoven, The Netherlands*
[3)]*General Atomics, 3550 General Atomics Ct, San Diego, California 90005, USA*
[4)]*Control Systems Technology, Department of Mechanical Engineering, Eindhoven University of Technology, P.O. Box 513, 5600 MB Eindhoven, The Netherlands*

(*Electronic mail: J.H.Slief@differ.nl)

(Dated: 5 July 2021)

I. INTRODUCTION

Radio frequency (RF) electromagnetic waves couple to charged particles in a plasma through resonant processes[1]. These resonances occur at specific values in plasma parameters, allowing a wave launched from a distance to couple into the core of a plasma confinement device, such as a tokamak. This coupling can impart not just energy, but momentum, altering the distribution function of electrons and/or ions, thereby driving currents. The application of RF power in the electron cyclotron (EC) range of frequencies results in particularly localized resonance, with high power EC waves stabilizing plasma instabilities in tokamaks such as neoclassical tearing modes by driving current within magnetic island structures as small as a few centimeters wide[2]. Recent studies have demonstrated that interactions between the propagating wave and plasma turbulence before it reaches any resonance can have a significant impact on the deposition profiles of the RF wave[3], but resolving this effect from plasma processes is a significant challenge. Fast transport in response to applied heating power can obscure the width of the power deposition profile[4]. Determining the full deposition profile therefore requires self-consistent treatment of applied power and the resulting transport[5,6]. To this end, Brookman et al. developed a method to self-consistently estimate power deposition and transport profiles from temperature measurements in response to a modulated RF heating source, denoted here as the 'flux-fit method'[7].

This letter presents a set of tools which improve on this method by addressing limitations and assumptions, which include limited freedom in the deposition profile estimation. One key assumption in[7] is that of a strictly Gaussian deposition profile with a fixed central deposition location determined by ray tracing, with only a variable width for fitting to the measured data. However, RF power deposition profiles need not, in general, be strictly Gaussian[8]. Reasons for this include misalignment of steering system or deformation of mirror due to extreme heat load[9]; modification of the original Gaussian beam shape due to local absorption, non-local redistribution of energy by resonant particles along the magnetic field line or intense focusing and strong wave interference[9]; or strong plasma inhomogeneity inside power deposition region[10]. Moreover, although ray tracing methods and experimental power deposition estimations generally agree well on the deposition location[11], in practice this is not always the case. Therefore, to accommodate for these deviations from a pure Gaussian profile with variable width only, extensions to the fitting model are required to increase the accuracy of the power deposition estimations using the flux-fit method. These extensions, in turn, require a different optimization procedure. In this letter, we present extensions to the flux-fit method as well as the new optimization procedure and we show how this improves the accuracy of the method.

II. ORIGINAL METHOD

In this section, we re-visit the flux fit method presented in[7] on which our extension is built. The original method, and our extended method, are based on the use of:

1. spatially and temporally resolved temperature perturbation measurements $\tilde{T}(\rho,t)$ resulting from a known modulated heat source $\tilde{U}(t)$,

2. a Gaussian parametrization of the expected source deposition profile $P(\rho)$,

with time t, $\rho = \sqrt{\psi_N}$ the square root of normalized toroidal flux (often referred to as 'normalized minor radius' and typically well approximated by $\rho \approx \frac{r}{a}$, with plasma minor radius a and r the distance from the magnetic axis).

The main difference between the work presented in this letter and in[7] is the freedom in the source profile parametrization, which also has consequences for the optimization.

In[7], the structure of the deposition profile is taken as a Gaussian fit of the TORAY-GA[12] ray-tracing code output, described by:

$$P(\rho) = A \exp\left(-\left(\frac{\rho - \mu_{\mathrm{TORAY}}}{\sigma_{\mathrm{TORAY}}}\right)^2\right), \qquad (1)$$

with estimated central deposition location μ_{TORAY} and width σ_{TORAY}. The resulting profile is convoluted with a Gaussian filter of width σ_F which results in a Gaussian profile at the

same peak location that is broadened by a (variable) factor b defined as:

$$b = \frac{\sqrt{\sigma_{\text{TORAY}}^2 + \sigma_F^2}}{\sigma_{\text{TORAY}}}. \tag{2}$$

This factor b is taken as a free parameter that is varied to determine the deposition profile $P(\rho, b)$. To determine the best fit for b, an iterative two-step procedure is used which involves calculating the perturbed heat-flux $\tilde{q}$.

Computing $\tilde{q}$ is based on the reduced one-dimensional heat transport equation, linearized around the quantities perturbed by the source (denoted with a tilde)[13]:

$$\frac{3}{2}\frac{\partial}{\partial t}\left(n(\rho)\tilde{T}(\rho,t)\right) = -\nabla_\rho \tilde{q}(\rho,t) + P(\rho)\tilde{U}(t), \tag{3}$$

where density $n(\rho)$ is assumed to be time-invariant and unaffected by the source perturbation but allowed to vary spatially. To circumvent having to compute the time derivative of measured temperature data in (3), which can introduce large errors, (3) is transformed into the frequency domain and re-expressed in terms of the perturbed heat flux, resulting in:

$$\tilde{Q}(\rho,\omega) = \frac{1}{\rho}\int_0^1 \rho' \left(\frac{3i}{2}\omega n(\rho')\tilde{\Theta}(\rho',\omega) - P(\rho',b)\tilde{\Upsilon}(\omega)\right) d\rho', \tag{4}$$

in cylindrical geometry[4,14], where $\tilde{\Theta}(\omega,\rho) = \mathscr{F}\{\tilde{T}(\rho,t)\}$ is the Fourier transform of the measured $\tilde{T}(\rho,t)$, $\tilde{\Upsilon}(\omega) = \mathscr{F}\{\tilde{U}(t)\}$ and $\tilde{Q}(\rho,\omega)$ the resulting (perturbed) heat flux in the frequency domain. Note that due to the linearity of (3), $\tilde{\Theta}(\rho,\omega)$ is independent for every perturbed frequency ω. Hence, $\tilde{Q}(\omega,\rho)$ can be computed independently for every frequency for a measured $\tilde{\Theta}(\rho,\omega)$ and a given $P(\rho,b)$.

In the next step, $\tilde{Q}(\omega,\rho)$, acquired using (4), is fit to a diffusive-convective model plus a coupled transport term dependent on the density modulation $\tilde{\nu}(\rho,\omega) = \mathscr{F}\{\tilde{n}(\rho,t)\}$:

$$\tilde{Q}(\omega)/n = -D_M \nabla_\rho \tilde{\Theta}(\omega) + V_M \tilde{\Theta}(\omega) + \xi(\omega), \tag{5}$$

where only the ω-dependency is made explicit since for the sake of concise notation, since all terms in 4 are dependent on ρ.

Consequently, given a certain b a $\tilde{Q}(\omega,\rho)$ can be found. Then, using the calculated $\tilde{Q}(\omega,\rho)$, (modulated) transport parameters D_M, V_M and ξ are fit across frequencies ω to find the best match to $\tilde{Q}(\omega,\rho)$. This procedure is repeated for multiple b, i.e., different broadened profiles, where the b are selected based on a grid. The χ^2 fit residuals for the various b are compared and the fit with minimal residual is selected as the best estimate for both the power deposition and transport profiles. Given that only one parameter needs to be optimized, b, this optimization approach is feasible. However, the use of a single free parameter in (1) places a severe restriction on the shape of profiles that can be estimated. Therefore, we propose an extension of the number of free parameters. With this, the total parameter space to be covered quickly explodes, such that a new optimization procedure is needed. The next section explains both the added free parameters and the new optimization procedure.

III. EXTENDED METHOD

The original flux fit method, as described in section II, is based on a Gaussian parametrization of the source deposition profile $P(\rho)$ using a single free parameter b. This severely restricts the freedom in the estimation of $P(\rho)$ and, therefore, we propose an extension to the number of free parameters, which will be explained in this section. Additionally, a new optimization procedure is needed to accommodate for the increased number of free parameters, which we will also explain here.

The new source profile parametrization is defined as:

$$P(\rho, b, \varsigma, A, \alpha) = R(\rho, b, \varsigma, A) S(\rho, \alpha), \tag{6}$$

which is comprised of the product of two functions R and S and contains four free parameters $(b, \varsigma, A, \alpha)$. R is an extension of (1) and is given by:

$$R(\rho, b, \varsigma, A) = A \exp\left(-\left(\frac{\rho - (\mu_{\text{TORAY}} - \varsigma)}{b\sigma_{\text{TORAY}}}\right)^2\right), \tag{7}$$

which, like (1) is a Gaussian with a variable width (described by b) but with the additional freedom in peak position (described by ς) as well as a variable peak height A. In this way, the definition of broadening factor b in (8) is altered to a simple scaling of the TORAY width:

$$b = \frac{\sigma_F}{\sigma_{\text{TORAY}}}, \tag{8}$$

where σ_F is the width of R.

To account for non-symmetric profiles (see e.g.[8,15]), R is multiplied by a skew function S with parameter α, given by:

$$S(\rho, \alpha) = 1 + \text{erf}\left(\alpha\left(\frac{\rho - \mu}{\sqrt{2\sigma_F^2}}\right)\right), \tag{9}$$

where erf denotes the error function and $\mu = \mu_{\text{TORAY}} - \varsigma$.

The new parametrization, $P(\rho, b, \varsigma, A, \alpha)$, replaces $P(\rho, b)$ in (4):

$$\tilde{Q}(\rho,\omega,b,\varsigma,A,\alpha) = \frac{1}{\rho}\int_0^1 \rho' \left(\frac{3i}{2}\omega n(\rho')\tilde{\Theta}(\rho',\omega) - P(\rho',b,\varsigma,A,\alpha)\tilde{\Upsilon}(\omega)\right) d\rho', \tag{10}$$

which is, again, fit to the right-hand side of (5). To find the optimal fit, however, we no longer make use of the two-step approach, since there are too many combinations of four fit

parameters to pick them from a grid of possible values. Instead, we use an iterative nonlinear least squares approach that fits $D_M(\rho), V_M(\rho)$ and $\xi(\rho)$, parametrized either by polynomials of arbitrary order or third-degree B-splines, to the parametrization of the perturbed heat flux $\tilde{Q}(\rho,\omega,b,\varsigma,A,\alpha)$:

$$[x,y] = \min_{x,y} \left|\left|\tilde{Q}(\rho,\omega,x) - y[\nabla_\rho \tilde{\Theta}(\rho,\omega), \tilde{\Theta}(\rho,\omega), 1]^{\mathrm{T}}\right|\right|^2, \tag{11}$$

where $x = [b,\varsigma,A,\alpha]$ and $y = [D_M(\rho), V_M(\rho), \xi(\rho)]$. The nonlinear optimization (11) is performed using the trust-region-reflective algorithm[16,17].

IV. SIMULATION RESULTS

In this section, we validate the extended estimation method, described in section III, by applying it to a set of simulated data and comparing with the original method with only a single free parameter in the source profile, b. The results are presented in this section.

A set of temperature perturbation data was generated using the models (4), (5) and artificial profiles for power deposition, diffusivity and convectivity (fig. 1). The P profile is a skewed, non-Gaussian function consisting of the positive part of a sine wave plus an exponential decay (see caption of fig. 1). The diffusivity and convectivity profiles are third order polynomials.

The estimation results for the original and extended methods are, respectively, shown in red dash-dot and blue dots. The D and V profiles estimated with the original method quite clearly deviate substantially from the simulated profiles, as they are trying to compensate for the large discrepancy between the estimated and simulated power deposition profiles. The extended method approximates the simulated profiles quite well, except in the region where significant power deposition occurs, where a deviation in D and V arises. Again, this is because there is a discrepancy between the estimated and simulated profiles (the latter non-Gaussian, the former a modified Gaussian) which needs to be compensated for in the fits of D and V. Moreover, due to the spatial integral definition of the flux that is fit (equation 4), discrepancies between the estimated and intrinsic deposition profiles also get integrated and the deviation of the transport estimates from the intrinsic profiles grows with radius. Due to this effect, it is hard to accurately estimate diffusivity and convectivity profiles with this method.

This, however, is found to be largely inconsequential to accurate source profile estimations. To support this, the sum of squared errors (SSE) between the estimated source profile using the extended flux fit method and the simulated profile was plotted against the SSE between the estimated diffusivity and the simulated profile, for polynomial orders of the estimated diffusivity profile ranging between 0 (constant over the entire domain) and 7. The SSE is defined by:

$$\mathrm{SSE}(\hat{X}_{Fluxfit}) = \sum_i^n \left(X_{sim}(\rho_i) - \hat{X}_{Fluxfit}(\rho_i)\right)^2, \tag{12}$$

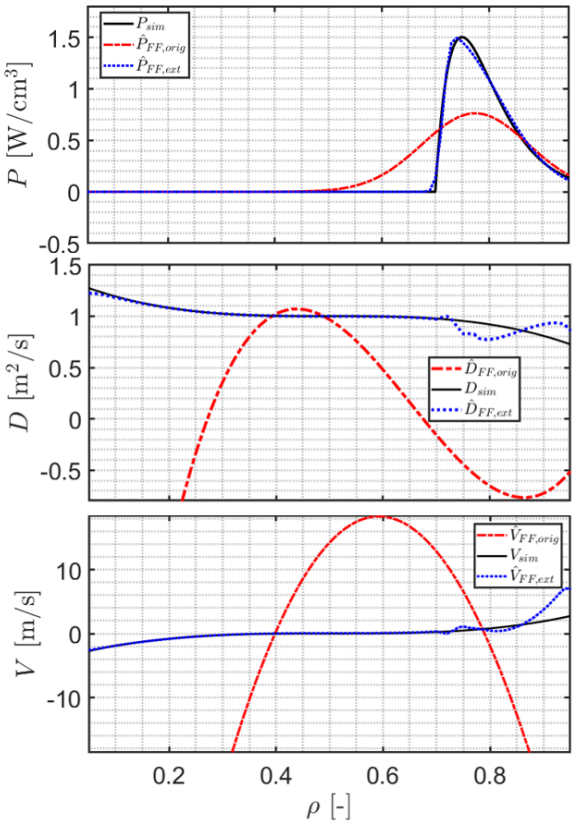

FIG. 1. Estimation of power deposition, diffusivity and convectivity profiles from a simulation (shown in black) of (3) with $\tilde{q}(\rho,t) = -D(\rho)\nabla_\rho \tilde{T}(\rho,t) + V(\rho)\tilde{T}(\rho,t)$, where $D(\rho) = -3(\rho - 0.5)^3 + 1$, $V(\rho) = 30(\rho - 0.5)^3$ and $P(\rho) = 52 * \max\left(\sin\left(0.5\pi(\rho - 0.7)\right), 0\right) \mathrm{e}^{(-20(\rho-0.7)+0.05)}$, comparing the resulting estimates from the original flux fit method[7] (denoted by FF,orig and shown in red dashes) to the extended flux fit method presented in this letter (denoted by FF,ext and shown in blue dots). The original flux fit implementation compensates for the skewed power deposition profile with a diffusivity and convectivity deviating substantially from the simulated profiles. The extended flux fit method is successful at estimating the correct diffusivity and convectivity profiles up to $\rho \approx 0.7$, where significant power is deposited.

where X_{sim} is the simulated profile, i.e. D_{sim} or P_{sim}, $\hat{X}_{Fluxfit}$ is the flux fit estimation of that same profile, n is the total number of spatial points and ρ_i is the ith spatial point.

The result, shown in fig. 2, shows that regardless the accuracy of the source (P) estimation is independent of the accuracy of the diffusivity (D) estimation. This implies that, provided we have sufficient freedom in the estimation of P, we can accurately estimate the deposition profile. However, errors made in the estimation thereof are compensated through the transport estimation, i.e., affect the estimated D and V. This supports the findings in[18,19]. Hence, the estimated D and V profiles will not necessarily reflect the intrinsic transport profiles and have little influence on the estimated deposition profile. Inversely, this implies that large errors made in the estimation of D and V reflect errors made in the estimation of P. With

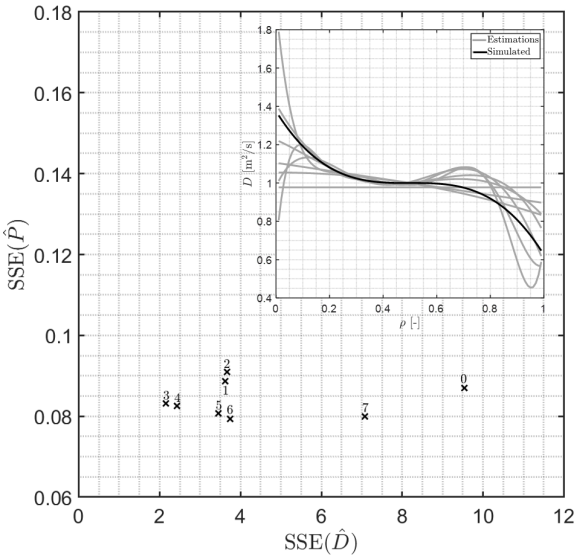

FIG. 2. Sum of squared errors (SSE) as defined by (12) of the extended flux fit power deposition estimation compared to a simulated profile like that of fig. 1, as a function of the diffusivity SSE for polynomial D estimations of order varying between 0 and 7. The simulated and esitmated D profiles are shown in the top right of the figure. The residual error between the estimated and simulated power deposition profiles is small and nearly independent of the accuracy of the diffusivity estimation.

prior knowledge of intrinsic transport profiles, any discrepancy between them and the estimated profiles might provide a hint that the estimated deposition profile might deviate from the intrinsic one. Without any such prior knowledge, large values (say, $D \gtrsim 1$ m^2/s and $|V| \gtrsim 10$ m/s in a DIII-D-sized tokamak) might provide the same.

V. EXPERIMENTAL RESULTS AND DISCUSSION

Here, the extended flux fit method is applied to real experimental data. We apply it to two datasets from DIII-D: shots 154532 (limited L-mode, $B_t = 2.0$ T, $I_p = 1.2$ MA, $n_{e,0} = 4.2 \times 10^{19}$ m^{-3}, $P_{inj,mod}$ = 3.0 MW and f_{mod} = 50 Hz) and 165078 (diverted L-mode, $B_t = 2.0$ T, $I_p = 1.0$ MA $n_{e,0} = 2.9 \times 10^{19}$ m^{-3}, $P_{inj,mod}$ = 1.0 MW and f_{mod} = 70 Hz), both analyzed in the original publication[7]). The modulated injected power $P_{inj,mod}$ is applied to the plasma by Electron Cyclotron Heating (ECH) and is modulated between 10 and 100% power. Fast Electron Cyclotron Emission (ECE) data (sampled at 500 kHz) is used to measure the resulting electron temperature perturbations through 40 channels corresponding to different spatial locations. Electron density measurements are provided by the DIII-D Thomson scattering diagnostic.

We apply and compare the following four power deposition estimation methods to the above shots:

- TORAY-GA[12],
- The extended flux fit method as presented in this letter (denoted by FF extended),
- The flux fit method where only b is varied (denoted by FF broadening only), to mimic the method as implemented by Brookman et al. in[7]
- Break-in-slope[20], as a reference for the two flux fit methods.

For shot 154532 the first 5 and for shot 165078 the first 3 harmonics of the modulation frequency were used in the flux fit estimations, corresponding to a signal-to-noise ratio (SNR) of ≥ 10 dB. Full width at half maximum (FWHM)[21].

These two shots are selected as illustrative examples of the importance of the added fit parameters in the extended flux fit method source function. Figure 3, for instance, shows the importance of allowing the freedom of peak location. The broadening-only method (denoted by the squares) is fixed in its peak location and can therefore only compensate for an apparent shift in peak power deposition location in the measurement data with respect to the TORAY estimation by substantial broadening to account for the measurement data. This shift could arise due to a variety of reasons, including deviations from local power absorption conditions in TORAY due to the power levels injected, plasma edge events temporarily shifting the TORAY estimated peak at the timestamp the profile was computed or inaccuracies in the mapping of temperature measurements to ρ. We define the broadening factor β as the ratio of full width at half maximum[21] (FWHM) of the flux fit estimate to the FWHM of the TORAY estimate (FWHMM$_{\text{TORAY}}$):

$$\beta = \text{FWHM}/\text{FWMH}_{\text{TORAY}}, \tag{13}$$

such that the broadening factor $\beta = 1$ when both curves are equally broad, $\beta > 1$ when the flux fit estimate is broader than the TORAY estimate and $\beta < 1$ when the flux fit estimate is less broad. Note that the FWHM of a Gaussian curve is proportional to its standard deviation σ, such that b in (8) and β in (13) are the same for Gaussian profiles.

The broadening-only estimate shows a broadening of $\beta = 2.7$ over TORAY due to its fixed peak position. The extended method (denoted by asterisks) finds a peak position shifted about 0.06 in ρ to the right (corresponding to about 4 cm in DIII-D). This peak position coincides with the peak estimated by the break-in-slope method (shown for reference as the dashed line), which is a method independent of any initial estimate of the profile. With the shift in peak position, the broadening with respect to the TORAY estimate is still significant (as observed by Brookman et al.[7]) but drastically reduced from $\beta = 2.7$ to 1.6.

The importance of including the skew parameter α is clearly illustrated in figure 4. In this particular case, allowing for a non-symmetric profile significantly reduces the broadening needed to fit the measurement data. Again, the broadening with respect to the ray tracing estimate observed in this shot

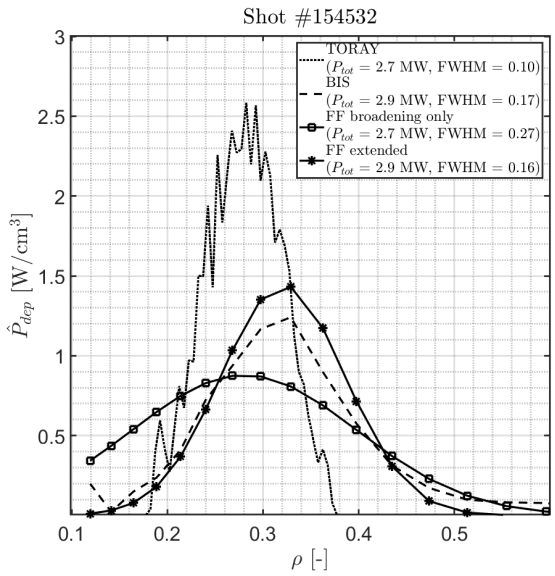

FIG. 3. Estimation of the power density deposited by modulated Electron Cyclotron Heating (ECH) as a function of normalized minor radius $\rho \approx a/r$ in DIII-D shot 154532. The broadening-only implementation of the flux fit method (FF broadening only) shows a broadened deposition profile with respect to the TORAY-GA[12] ray tracing estimate. The extended flux fit method (FF extended), presented in this work, shows a less severe broadening by allowing for freedom in the peak location. A break-in-slope (BIS) estimate is shown for comparison.

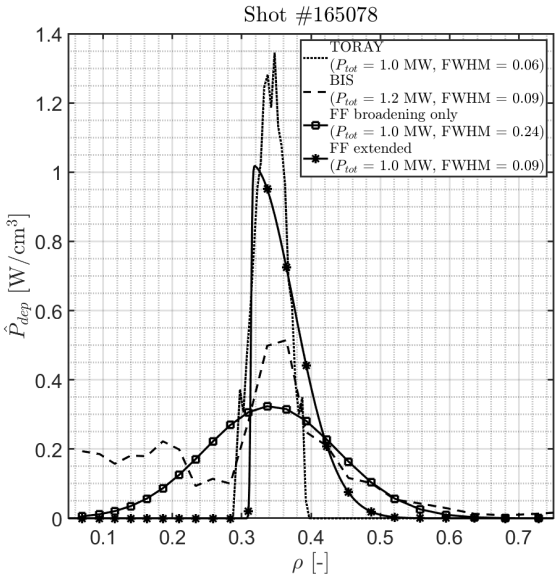

FIG. 4. Estimation of the power density deposited by modulated Electron Cyclotron Heating (ECH) as a function of normalized minor radius $\rho \approx a/r$ in DIII-D shot 165078. The broadening-only implementation of the flux fit method (FF broadening only) shows a broadened deposition profile with respect to the TORAY-GA[12] ray tracing estimate. The extended flux fit method (FF extended), presented in this work, shows a less severe broadening by allowing for a skewed Gaussian profile. A break-in-slope (BIS) estimate is shown for comparison.

in previous work[7] remains, yet is considerably reduced from $\beta = 4.0$ when only the broadening is allowed to be varied to $\beta = 1.5$ in the extended method with all four parameters.

Note that Brookman et al. report a broadening of 2.2 according to the definition in (8) for this shot, which deviates from the 4.0 broadening factor for the broadening-only method in figure 4. Most likely, this is due to the differences in implementation between the implementation presented in this work and that of Brookman et al.[7]. Moreover, the raw data stems from the same shot but was processed independently. Despite this difference, the significant reduction in observed broadening when allowing for a skewed profile estimation remains.

For completeness, we also want to note that there are alternative (exotic) explanations for a broadening effect due to fast non-local transport mechanisms. This would (also) lead to a broadening of the deposition profile as estimated using the methodologies presented here[14].

VI. CONCLUSION

This work presents an extension to the 'flux fit' method[7] for estimating power deposition profiles and spatially varying modulated heat transport coefficients (diffusivity and convectivity) based on temperature measurements from a periodically perturbed source and a parametrization of its expected spatial profile. The original work considered strictly Gaussian power deposition profiles, with a variable width (standard deviation) used for fitting.

A purely Gaussian profile with its width the only free parameter provides insufficient freedom to accurately estimate source deposition profiles in all cases. Therefore, in this work, the number of parameters available for fitting of the source function is extended to include a variable peak location, peak height, and a skewness parameter. With this extension, the original orthogonal distance regression procedure for finding the optimal fit for the free parameter, consisting of a grid search-like approach, is no longer suitable. The optimization procedure is therefore changed to a nonlinear least squares optimization.

This method is applied to two of the discharges used in the original publication to show that the inclusion of these extra degrees of freedom has a significant impact on the resulting source profile estimate. In both cases, a broadening compared to ray tracing estimates is observed (1.6 and 1.5 times for shots 154532 and 165078, respectively) but to a lesser extent than previously estimated (respectively 2.7 and 2.2 times[7]).

It is shown that, in the method presented in this work, the quality of the estimated deposition profile is key to the accuracy of diffusivity and convectivity estimates, but, inversely, the estimated transport parameters hardly affect the quality of the power deposition estimate. We therefore conclude the extended method presented in this work is suitable for power

deposition estimates irrespective of the estimated transport parameters, but unsuitable for accurate estimation of the latter.

DATA AVAILABILITY STATEMENT

Raw data were generated at the DIII-D large scale facility. Derived data supporting the findings of this study are available from the corresponding author upon reasonable request.

[1] V. Erckmann and U. Gasparino, "Electron cyclotron resonance heating and current drive in toroidal fusion plasmas," Plasma Physics and Controlled Fusion **36**, 1869–1962 (1994).

[2] G. Gantenbein, H. Zohm, G. Giruzzi, S. Günter, F. Leuterer, M. Maraschek, J. Meskat, and Q. Yu, "Complete suppression of neoclassical tearing modes with current drive at the electron-cyclotron-resonance frequency in ASDEX upgrade tokamak," Physical Review Letters **85**, 1242–1245 (2000).

[3] O. Chellaï, S. Alberti, M. Baquero-Ruiz, I. Furno, T. Goodman, F. Manke, G. Plyushchev, L. Guidi, A. Koehn, O. Maj, E. Poli, K. Hizanidis, L. Figini, and D. Ricci, "Millimeter-wave beam scattering by field-aligned blobs in simple magnetized toroidal plasmas," Physical Review Letters **120**, 105001 (2018).

[4] U. Stroth, L. Giannone, and H. J. Hartfuss, "Fast transport changes and power degradation in the W7-AS stellarator," Plasma Physics and Controlled Fusion **38**, 611–618 (1996).

[5] M. Van Berkel, T. Kobayashi, G. Vandersteen, H. J. Zwart, H. Igami, S. Kubo, N. Tamura, H. Tsuchiya, and M. R. De Baar, "Heat flux reconstruction and effective diffusion estimation from perturbative experiments using advanced filtering and confidence analysis," Nuclear Fusion **58**, 096036 (2018).

[6] K. W. Gentle, M. E. Austin, J. C. Deboo, T. C. Luce, and C. C. Petty, "Electron energy transport inferences from modulated electron cyclotron heating in DIII-D," Physics of Plasmas **13**, 1–8 (2006).

[7] M. W. Brookman, M. E. Austin, C. C. Petty, R. J. La Haye, K. Barada, T. L. Rhodes, Z. Yan, A. Köhn, M. B. Thomas, J. Leddy, and R. G. L. Vann, "Resolving ECRH deposition broadening due to edge turbulence in DIII-D," Physics of Plasmas **28**, 42507 (2021).

[8] E. Westerhof, "Electron cyclotron waves, transport and instabilities in hot plasmas," (1987).

[9] C. Tsironis, E. Poli, and G. V. Pereverzev, "Beam tracing description of non-Gaussian wave beams," Physics of Plasmas **13**, 113304 (2006).

[10] A. A. Balakin, M. A. Balakina, and E. Westerhof, "ECRH power deposition from a quasi-optical point of view," Nuclear Fusion **48**, 065003 (2008).

[11] M. Zerbini, M. Austin, S. Bernabei, G. Giruzzi, M. Murakami, and J. Lohr, "Correlation analysis of 110 GHz ECH modulation experiments on the DIII-D tokamak," Tech. Rep. (1999).

[12] R. Prater, D. Farina, Y. Gribov, R. W. Harvey, A. K. Ram, Y. R. Lin-Liu, E. Poli, A. P. Smirnov, F. Volpe, E. Westerhof, and A. Zvonkov, "Benchmarking of codes for electron cyclotron heating and electron cyclotron current drive under ITER conditions," Nuclear Fusion **48**, 035006 (2008).

[13] N. J. Cardozo, "Perturbative transport studies in fusion plasmas," Plasma Physics and Controlled Fusion **37**, 799–852 (1995).

[14] M. Van Berkel, G. Vandersteen, H. J. Zwart, G. M. Hogeweij, J. Citrin, E. Westerhof, D. Peumans, and M. R. De Baar, "Separation of transport in slow and fast time-scales using modulated heat pulse experiments (hysteresis in flux explained)," Nuclear Fusion **58**, 17 (2018).

[15] E. Westerhof and W. J. Goedheer, "Transport code studies of m=2 mode control by local electron cyclotron heating in TFR," Plasma Physics and Controlled Fusion **30**, 1691–1699 (1988).

[16] T. Coleman and Y. li, "On the convergence of reflective newton methods for large-scale nonlinear minimization subject to bounds," Math. Program. **67**, 189–224 (1994).

[17] T. F. Coleman and Y. Li, "An interior trust region approach for nonlinear minimization subject to bounds," SIAM Journal on Optimization **6**, 418–445 (1996).

[18] M. van Berkel, G. W. Oosterwegel, G. Vandersteen, H. J. Zwart, G. Hogeweij, E. Westerhof, and J. Citrin, "Simultaneous estimation of transport and power deposition profiles," in *46th European Physical Society Conference on Plasma Physics (EPS 2019)* (DIFFER, Milan, 2019).

[19] B. H. van den Boorn, *Sensitivity analysis of the heat transport coefficient estimation in fusion reactors and their identifiability under noisy conditions*, Ph.D. thesis, Eindhoven University of Technology (2021).

[20] E. A. Lerche and D. Van Eester, "Improved break-in-slope analysis of the plasma energy response in tokamaks," Plasma Physics and Controlled Fusion **50**, 035003 (2008).

[21] M. H. Weik, "full-width at half-maximum," in *Computer Science and Communications Dictionary* (Springer US, Boston, MA, 2001) pp. 661–661.

Chapter 4

Numerical validation of estimation methods

Prior to application on experimental data, the implementation of the different estimation methods should be tested and validated. Hence, data sets are simulated with different simulated power deposition and diffusivity profiles to which the different estimation methods are applied. This allows comparison of the estimated and simulated profiles to evaluate the accuracy of the estimation methods and under which conditions they perform well. This chapter presents the estimation results and the implications that these have for the estimations on real measurement data.

4.1 Simulated test data

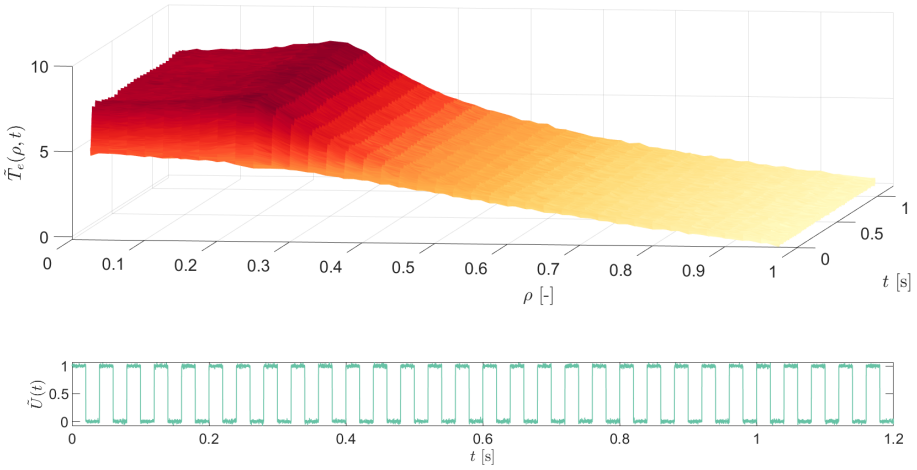

FIGURE 4.1: Surface plot of simulated electron temperature $T_e(\rho, t)$ from solving (2.18) with a constant diffusion coefficient profile, modulated power source with Gaussian profile centered at $\rho = 0.25$, mixed Neumann-Dirichlet boundary conditions and additive time-domain white Gaussian noise.

To validate the estimation methods, they are applied to simulated test data. This data is generated by solving (2.18) with $V = K = 0$ and D constant over ρ (its value will differ per case, see section 4.1.1). Moreover, the electron density n_e is assumed constant in time and space so that it can be easily factored out. $U(t)$ is a block wave varying between 1 (full power) and 0 (no power) with frequency f_0, equal to 25 cycles per unit time. The boundary conditions are $\frac{\partial \tilde{T}_e(\rho=0,t)}{\partial t} = 0$ and $\tilde{T}_e(\rho = 1, t) = 0$. Filtering and processing is done according to section 3.1. Normally distributed white noise is added to both $\tilde{T}_e$ and $\tilde{U}$ in the time domain to simulate real measurements. The resulting solution for the temperature perturbation in time and space is shown in figure 4.1. The bottom window shows $\tilde{U}$.

A typical spectrum for a perturbative experiment is shown in figure 4.2, showing the simulated amplitude and phase of the complex temperature perturbation Fourier coefficients Θ, of the first four excited harmonics. The input signal, a block wave, excites only odd harmonics of the fundamental frequency, at 25 Hz. A peak in amplitude is visible at the power deposition location ($\rho = 0.25$) as well as the subsequent drop-off of magnitude with increasing steepness for increasing frequencies, until the noise floor is reached.

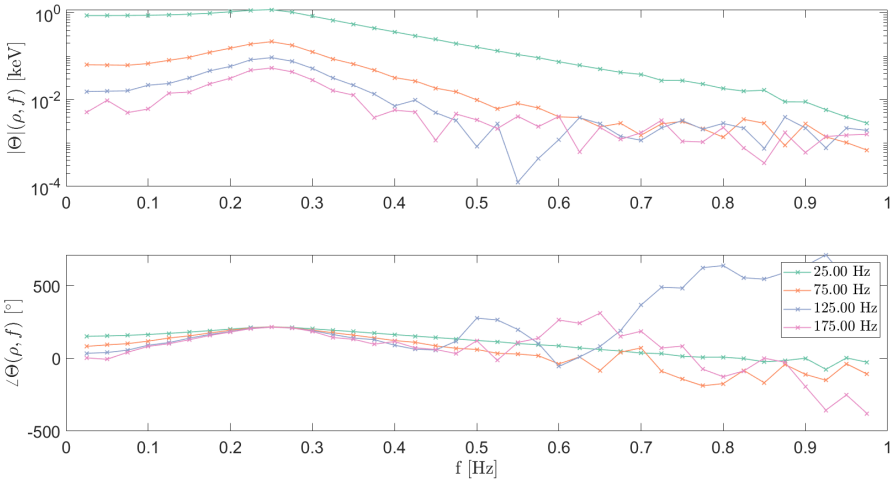

FIGURE 4.2: The spatial profile of the magnitude of Fourier coefficients for the first four excited frequencies, shows how at the deposition location ($\rho = 0.25$) the magnitude peaks and then drops off with a constant slope that becomes steeper with increasing frequency. The phase converges to the same value at the deposition location. All frequencies, in both magnitude and phase, become increasingly erratic further away from the source, due to a low signal-to-noise ratio.

4.1.1 Deposition profile estimation

In this section, deposition profile estimations for three methods are shown for three different cases, based on the simulated data described above. The estimation methods are the FFT method, the break-in-slope method and the MLE method, the three oldest methods used in this thesis. After this, simulations including the state-of-the-art methods (FDLS, flux fit) will be presented.

All cases have a narrow ($\sigma = 0.05$) Gaussian deposition profile centered either at $\rho = 0.5$ (figures 4.4 and 4.3) or 0.1 (figure 4.5). The level of diffusion is either high ($D = 8$ m^2/s) or low ($D = 1$ m^2/s). On the left, the figures show the simulated deposition profile in black and estimations from the three different techniques in different colors and marker shapes. In the break-in-slope case, the confidence bounds indicated are the sum of squared error (SSE) values from the fits that are made to determine the slope at the break points. The FFT and MLE confidence bounds are given by two standard deviations. The right figures show the simulated diffusion coefficient (dashed black line) and the diffusion coefficient as estimated by the MLE in red.

For small diffusion coefficient values, the break-in-slope and MLE methods agree and estimate the deposition profile well, barring large MLE uncertainties at the edges of the domain. When diffusion is large, however, the break-in-slope estimation is artificially broadened by the fast dissipation of heat the moment it is deposited. In contrast, the MLE still estimates very accurately since it simultaneously estimates the diffusion coefficient and corrects for the broadening effect. This is seen also when deposition is moved close to the inner domain boundary. The MLE estimates the points on the deposition profile well compared to the break-in-slope, in which the effects of the Neumann boundary condition at $\rho = 0$ can be seen. The FFT method clearly performs the poorest out of the three under these circumstances. It does well at estimating the peak location of deposition, but not its height or width. This is unsurprising given the

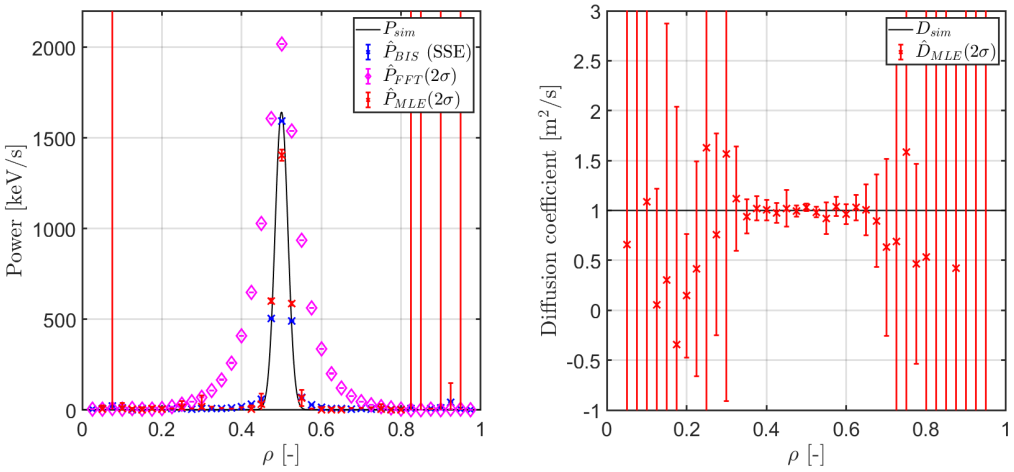

FIGURE 4.3: On the left: at transport levels expected in current-day tokamaks (here, diffusivity $D = 1$ m^2/s) the BIS (blue crosses) and MLE (red crosses) methods estimate very well the simulated deposition profile (black). The FFT method (pink diamonds) does not perform well, showing significant broadening with respect to the simulated profile. On the right: the diffusivity profile is estimated poorly by the MLE method.

assumptions behind the FFT method; it is reliable for high modulation frequencies, when transport can be neglected compared to the source (section 3.1.1). Clearly the simulated modulation frequency of 25 Hz is not high enough to fulfill this assumption.

It is also concluded that the MLE performs the best in estimating power deposition between the three methods, followed by the break-in-slope method which performs well when diffusion is not larger than approximately 2 m^2/s. A last conclusion that can be drawn from these simulations is that diffusivity is not well estimated by the MLE method. Rather, the diffusivity compensates for errors made in the estimation of P, allowing for a good power deposition estimate but simultaneously causing large error bars and fluctuations in the diffusivity estimate.

Due to the poor performance of the FFT method in the context of the simulations presented here, which have been set up so as to mimic as closely as possible the experimental conditions of DIII-D discharges presented in chapter 5, the FFT method has been left out in subsequent chapters in favor of the two state-of-the art estimation techniques: the FDLS and flux fit methods. These methods, two relatively old ones in the MLE and BIS and two very new ones, are compared for a rather extreme case in figure 4.6, a case with a distinctly non-Gaussian and heavily skewed deposition profile and with the inclusion of white noise on the data. The three newest methods (MLE, FDLS and FF) still estimate the profile very well, but the BIS is broadened. This is expected from the simulation results shown just prior. The FF method shows significant error bars in the heavily skewed section of the deposition profile, which is due to the implementation of the error estimate for this method; uncertainties are assumed to be independent for each of the four estimated parameters in the FF deposition profile and therefore added when, in reality, these uncertainties are not independent. This leads to an overestimation of the uncertainty bounds. A proper handling of these uncertainties will be implemented in the future.

4.1.2 Effect of transport estimations on deposition estimation

In figure 2, section 3.3, it was shown that, for the flux fit method, there is little influence of the estimated transport parameters on the accuracy of the power deposition estimate. This was done by estimating

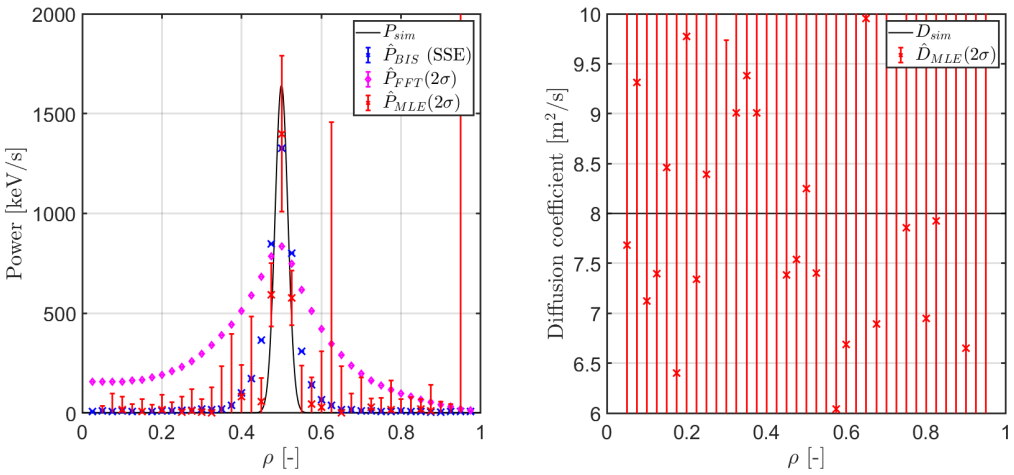

FIGURE 4.4: The FFT (pink diamonds) and BIS (blue crosses) methods perform relatively poorly in estimating the simulated deposition profile (black) at elevated levels of transport (here, $D(\rho) = 8$ m^2/s over the entire domain) (left figure). In contrast, the MLE estimate (red crosses) estimates power deposition well even in the presence of high transport. This comes at the cost of great uncertainty in the diffusivity estimate (right figure).

D and P, where D was simulated using a cubic polynomial while the estimation of D was done using polynomials of order varying between 0 and 7. The same has also been done for the FDLS method; the result is shown in figure 4.7. It can be seen that the error in the estimated D profile for the FLDS method varies even more than the flux fit D estimate, yet there is even fewer variance in the FDLS P estimate, indicating that the FDLS power deposition estimation is even less sensitive to the estimated transport than the flux fit method. This corresponds well with the findings in [80], which shows similarly for the MLE method that the estimation of P is by far the most accurate and reliable.

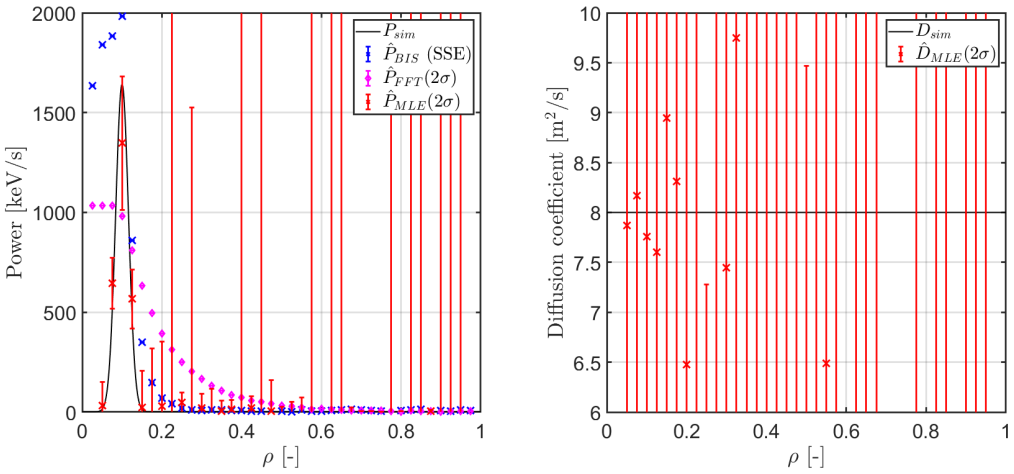

FIGURE 4.5: On the left: the simulated deposition profile (in black) close to the edge of the domain is poorly estimated by both BIS (blue crosses) and FFT (pink diamonds) methods, but well by the MLE method (red crosses). On the right: the diffusivity estimate by the MLE method is uncertain, inaccurate and imprecise.

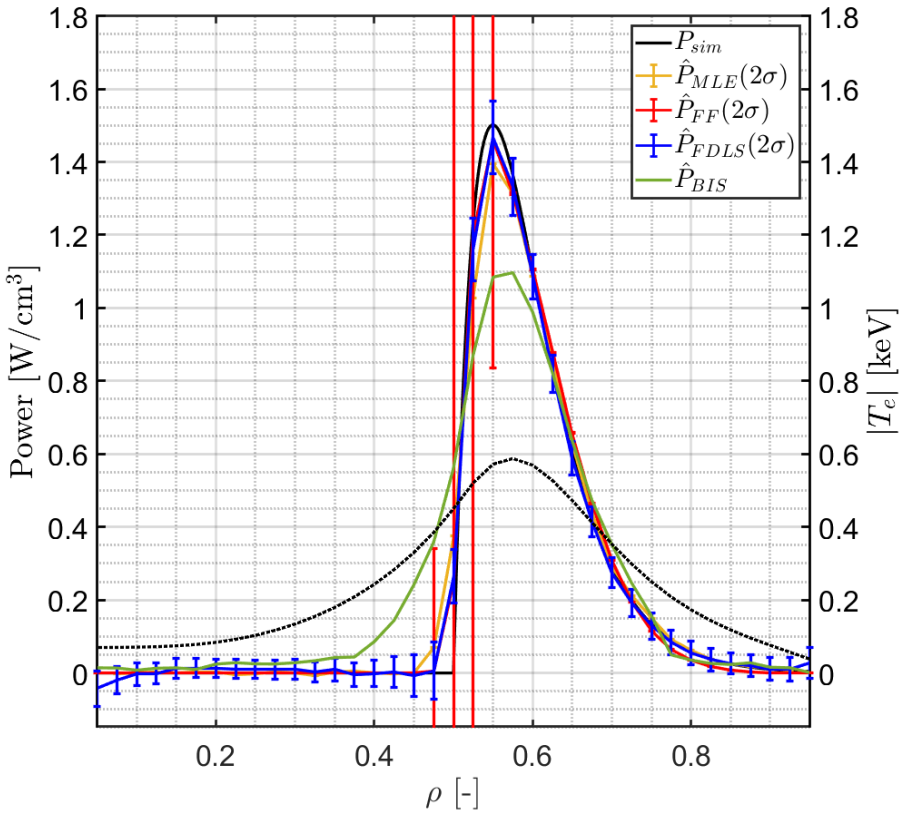

FIGURE 4.6: The MLE, FDLS and FF methods estimate this non-Gaussian, heavily skewed simulated deposition profile (black) well based on simulated temperature data with added normally distributed white noise. The break-in-slope estimate is broadened towards the skewed side of the profile.

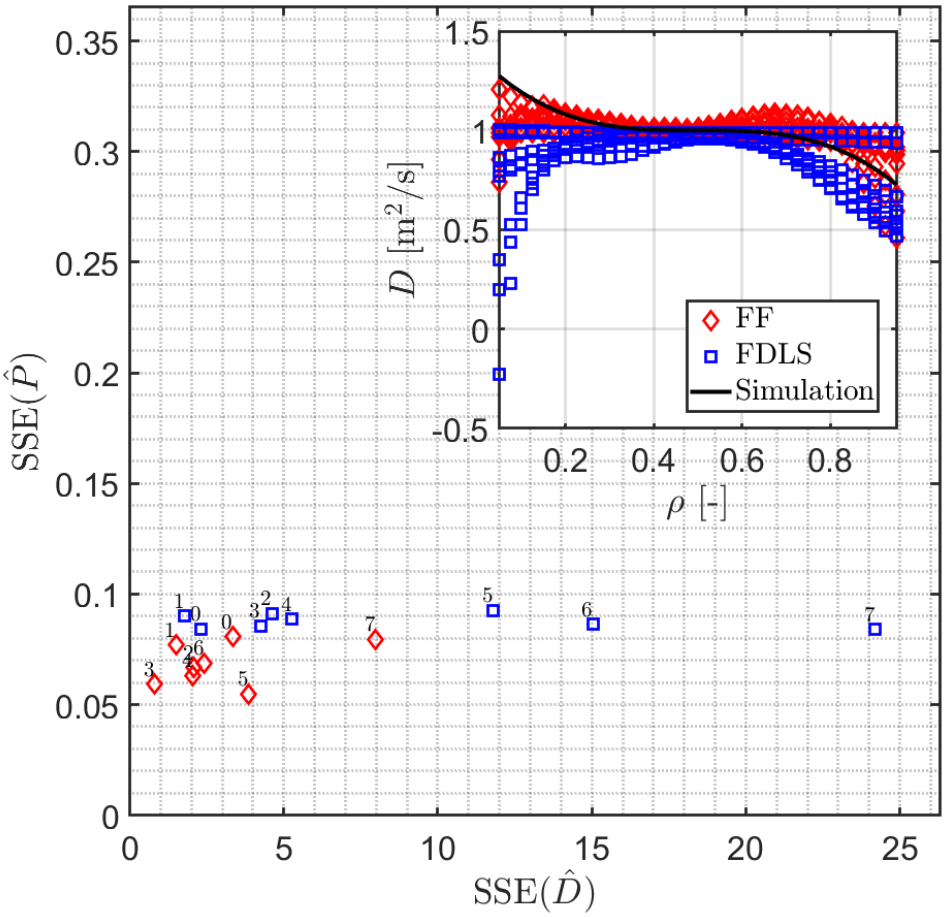

FIGURE 4.7: The accuracy of the FDLS and FF estimations of the power deposition profile $\hat{P}$ is small compared to the peak deposited power (here 1.5 W/cm^3) and independent of the accuracy in the diffusivity profile $\hat{D}$, as measured by the sum of squared errors (SSE) between the estimated and simulated profiles, since the total error in the power deposition estimate $SSE(\hat{P})$ does not vary significantly with the error in the diffusivity $SSE(\hat{D})$. D is simulated using a third order polynomial while it is estimated using polynomials or order varying between 0 and 7. The simulated and estimated D profiles are shown in the top right of the figure.

Chapter 5

Experimental deposition profile estimation results

In this chapter, the results of applying the methods detailed in section 2.6 to temperature measurements from various DIII-D discharges is presented. Before the results, the data is introduced and a brief note on the assumptions of non-perturbed density and linearity is made.

5.1 DIII-D data

Figure 5.1 shows a typical example of measurement data used in this work. It shows a surface plot of calibrated ECE measurement data for a particular discharge (154532 [27]) over time and mapped to the dimensionless minor radius coordinate ρ. The ECE system measures the electron temperature through 48 channels. This discharge is a limited L-mode discharge without significant sawtoothing [1]. 3 MW of ECH power is injected near $\rho = 0.5$, modulated between full power and 10% power at 50 Hz with a 50% duty cycle. Typically in modulated DIII-D discharges, injected power lies between 0.5 and 3 MW, deposited between $\rho = 0.2$ and 0.7, modulated between 25 and 100 Hz.

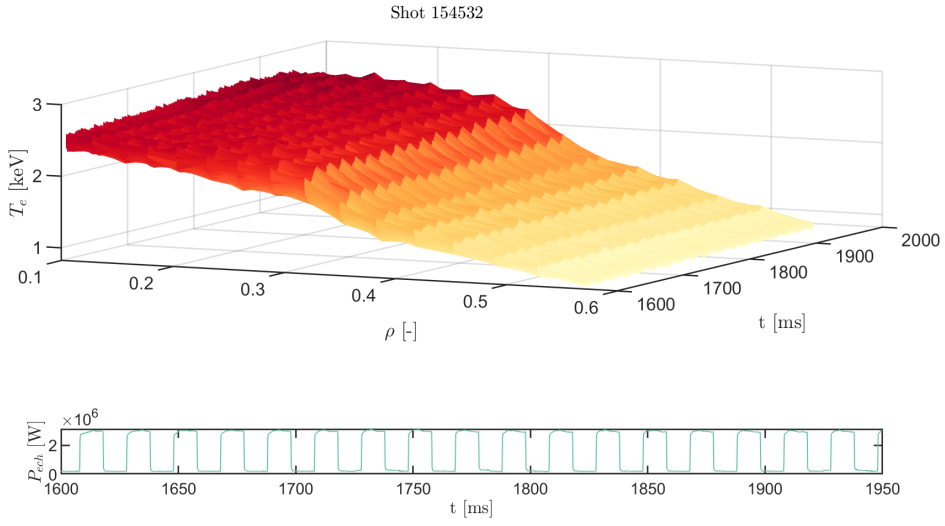

FIGURE 5.1: Calibrated electron temperature data of DIII-D discharge no. 154532 (Limited L-mode, $B_T = 2.0$ T, $I_p = 1.2$ MA, $n_{e,0} = 4.2{\times}10^{19}$ m^{-3} [27]) as a function of time t and flux surface label ρ. The injected modulated ECH power $P_{ech}(t)$ is shown in the bottom plot.

[1] The sawtooth instability is an instability found in the core of tokamak plasmas where the temperature signal measured at a certain location looks like a sawtooth; i.e. (semi-)periodic build up of temperature followed by a crash [81].

5.2 Validation of assumptions

The estimation methods that are used to obtain the results that are presented in this chapter, described in section 2.6, are based on a number of assumptions. Validating that these assumptions hold true gives confidence in their outcomes. Two of the most important assumptions are that the temperature perturbation caused by the modulated ECH source is linear and that the electron density remains unperturbed. Checking these assumptions requires specific experimental conditions that are not present in all discharges, making them difficult to check in general. Nevertheless, they are present in two specific discharges that are therefore used to validate these assumptions. The results are discussed in this section.

5.2.1 Assumption of non-perturbed density

All experimental estimation methods presented and applied in this work assume that ECH modulation applied to the plasma induces a temperature perturbation but does not significantly perturb the density, which in a steady-state plasma is therefore constant in time. Checking the assumption requires 1) time-resolved electron density measurements with a sample frequency that is large enough compared to the modulation frequency and 2) the ECH power deposition location within the spatial measurement range of the diagnostic. This combination of conditions was found for a single discharge out of those analyzed, number 174673. The Thomson scattering density and amplitude spectra for this discharge are shown side by side in figure 5.2. In figure 5.2b, a clear temperature perturbation is seen at the ECH modulation frequency. In contrast, no clear density perturbation is seen at the same frequency, or, in fact, at any frequency, in figure 5.2a. This confirms the assumption that the electron density is not affected by the ECH modulation for this discharge. This gives some confidence that this will hold true for other discharges.

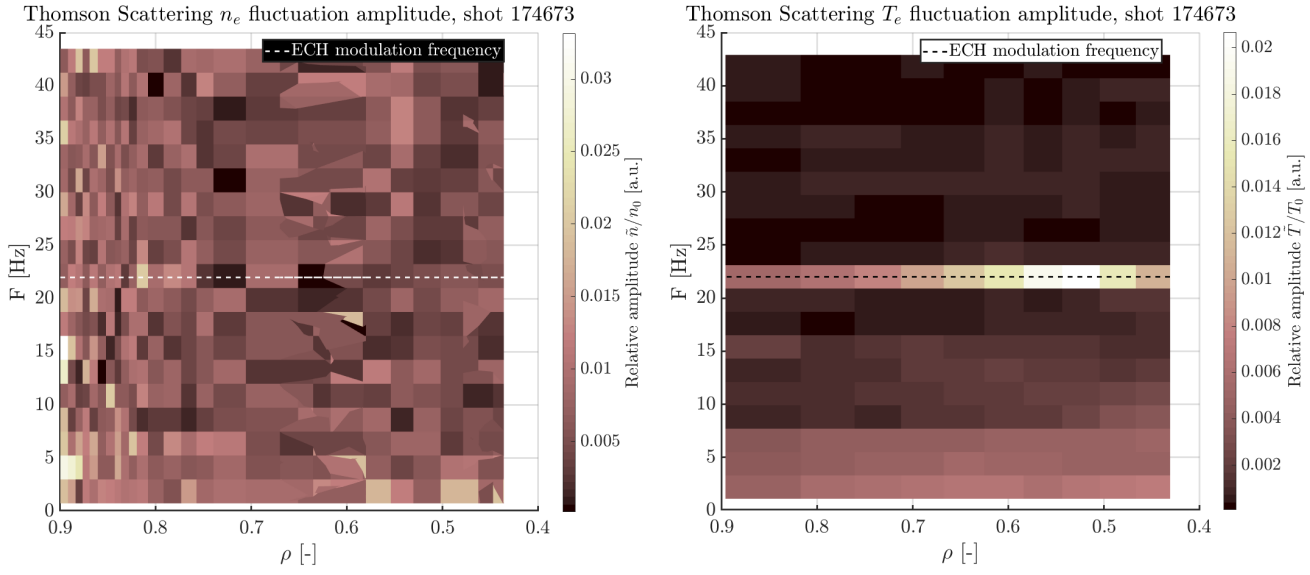

(A) (B)

FIGURE 5.2: Evidence for the assumption that density is not perturbed by the modulated ECH source in this discharge (174673), as can be see from the significant fluctuation amplitude in the electron temperature (B) at the ECH modulation frequency (black dotted line) but not at surrounding frequencies, across the plasma, while the same significant fluctuation amplitude is not seen in the density spectrum (A). Both are measured using Thomson scattering.

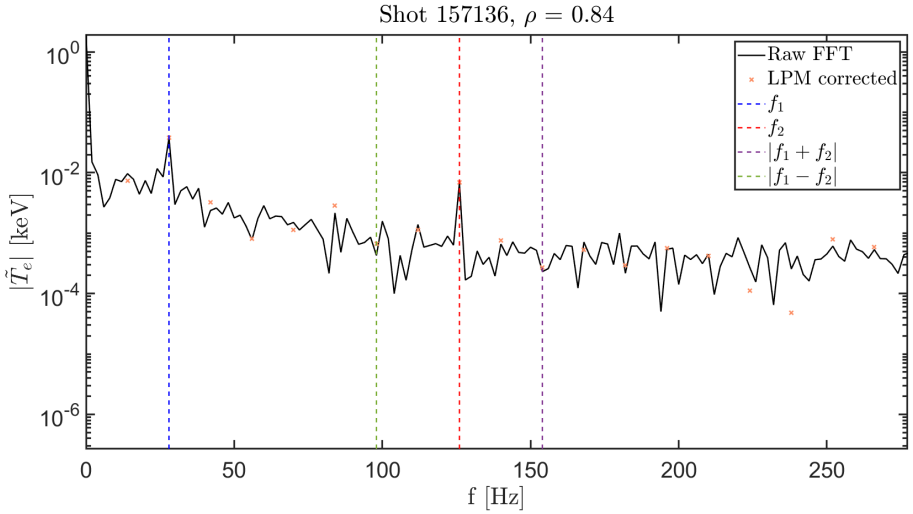

FIGURE 5.3: The electron temperature amplitude spectrum from DIII-D discharge 157136 at $\rho = 0.84$ indicates that the perturbations caused by the two perturbing frequencies, f_1 and f_2, is linear to a good approximation, since the sum and difference frequencies (f_1 and f_2) are not visible.

5.2.2 Assumption of linearity

All estimation methods in this thesis rely on the linearization of the transport equation, under the assumption that the perturbation caused by the source is sufficiently small so that the response is linear. The easiest test to this assumption is to increase the strength of the perturbing source by some factor and see if the temperature perturbation amplitude is multiplied by the same factor. Unfortunately, no single discharge was found where, within the same discharge, this was done.

A slightly more involved way to test this assumption is using the so-called two-tone test. A nonlinear system excited by two frequencies f_1 and f_2 will produce a response at sum and difference frequencies $f_1 \pm f_2$, too. A linear system, in contrast, will not. For one particular discharge, number 157136, two gyrotrons were modulated with two different frequencies at the same plasma location. Therefore, it is possible to check the linearity assumption using the two-tone test for this discharge.

The temperature amplitude spectrum for one particular location in discharge 157136 is shown in figure 5.3. Note that this was done for all ρ between 0 and 1, so the below argument holds even though only a single illustrative location is shown.
A special implementation of the LPM (section 3.1.3) that was adapted to handle this type of dual perturbation frequency spectrum, the two-tone LPM [79], was applied to the spectrum, shown by the orange crosses. The two perturbing frequencies, f_1 and f_2, are clearly visible in the spectrum while there are no peaks visible at $f_1 \pm f_2$. Either these are not excited or their excitation is weak enough to be buried in noise; either way, the assumption of linearity seems to hold in this discharge at least for the first harmonics of both frequencies.

5.3 Estimation results

Six total discharges are analyzed; the estimations for their power deposition profiles are presented in this section. Five of these discharges (154532, 157131, 165078, 165146 and 166192) are chosen based on [27], wherein their broadening with respect to TORAY-GA is analyzed. These discharges are selected as typical examples of different discharge modes in DIII-D: a limited L-mode (154532), diverted L-mode (165078), QH-mode (157131), ELMy H-mode (165146) and a negative triangularity (166192) discharge. One additional dicsharge (174673), another QH-mode, is analyzed.

5.3.1 Defining broadening

In [27] the Gaussian filter-based broadening factor b_{GF} is defined as:

$$b_{GF} = \frac{\sqrt{\sigma_F^2 + \sigma_{TORAY}^2}}{\sigma_{TORAY}}, \tag{5.1}$$

with σ_{TORAY} the standard deviation of a Gaussian fit of the TORAY estimate of the power deposition profile and σ_F the width of a power conserving Gaussian filter that is convolved with the TORAY estimate to obtain profile that is broadened but still Gaussian. In this work, neither the TORAY profiles nor the experimental ones are assumed to be Gaussian, so the broadening factor b is defined as the ratio of Full Width at Half Maximum (FWHM) [82] of the experimental estimate to that of the TORAY estimate:

$$b = FWHM/FWHM_{TORAY}. \tag{5.2}$$

For a Gaussian profile, $FWHM = 2\sqrt{2\ln 2}\sigma$ [83]. For Gaussian profiles, therefore, (5.2) may be equivalently written as the ratio of the standard deviation (SD) of the filter and TORAY profiles as they are defined in [27]:

$$b_{SD} = \sigma_F/\sigma_{TORAY}. \tag{5.3}$$

This definition is equivalent to (5.1):

$$b_{SD} = \sqrt{b_{GF}^2 - 1}. \tag{5.4}$$

In [27], the broadening factors observed for the five discharges range between $b_{GF} = 1.5$ - 3, or, equivalently, $b_{SD} = 1.1$ - 2.8. Here, the same discharges are found to have broadening factors b between 1.0 (for 165146) and 6.2 (for 157131). The final discharge (174673) lies within that range at b between 1.8 and 2.9 for the different estimates. The estimates for all discharges are shown in figure 5.4, with the FWHM of the TORAY estimate shown in terms of $\rho \approx r/a$ with $a \approx 0.67$ m. The dashed line shows the electron temperature spatial amplitude profile of the first perturbed harmonic for reference. While these results speak for themselves, the most interesting observations will be highlighted below. A full overview of the results from figure 5.4 is presented in table 5.1 for completeness. A summary of the results is foud in table 5.2.

TABLE 5.1: Summary of the results in figure 5.4 with b according to (5.2) and b_{SD} according to (5.3) for those discharges analyzed in Brookman *et al.* [27].

	b (MLE - FF - FDLS - BIS)	b_{SD} [27]	P_{tot} [MW] (TORAY - MLE - FF - FDLS - BIS)
Limited L-mode (154532)	1.7 - 1.6 - 1.6 - 1.8	2.72	2.7 - 3.1 - 2.9 - 2.6 - 2.8
Diverted L-mode (165078)	1.5 - 1.6 - 1.4 - 1.6	2.24	1.0 - 0.7 - 0.9 - 0.8 - 0.9
QH-mode (157131)	- 4.4 - - 6.2	2.00	0.5 - 0.3 - 0.5 - 0.3 - 0.5
QH-mode (174673)	2.4 - 1.8 - 2.5 - 2.9	-	0.5 - 0.7 - 0.8 - 0.7 - 0.9
ELMy H-mode (165146)	1.4 - 1.0 - 1.3 - 2.0	1.67	2.9 - 4.4 - 3.5 - 3.6 - 4.3
-δ L-mode (166192)	3.3 - 3.3 - 2.6 - 3.6	1.30	0.6 - 0.6 - 0.7 - 0.6 - 0.7

5.3.2 Results

Looking at figure 5.4, in general, all four estimation methods (MLE, FF, FDLS and BIS) agree quite well in their profile estimations. The biggest deviations occur in the BIS estimations, which tends to be slightly broader than the other methods, with somewhat underestimated peak power levels. This falls within the expectation for this method. Other than that, there is some discrepancy in discharges 174673

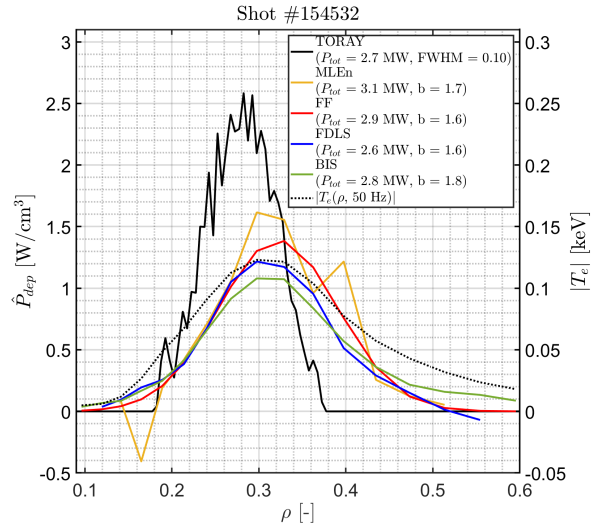

(A) DIII-D discharge 154532 (limited L-mode, B_T = 2.0 T, I_p = 1.2 MA, $n_{e,0}$ = 4.2×10^{19} m^{-3}, P_{mECH} = 2.7 MW)

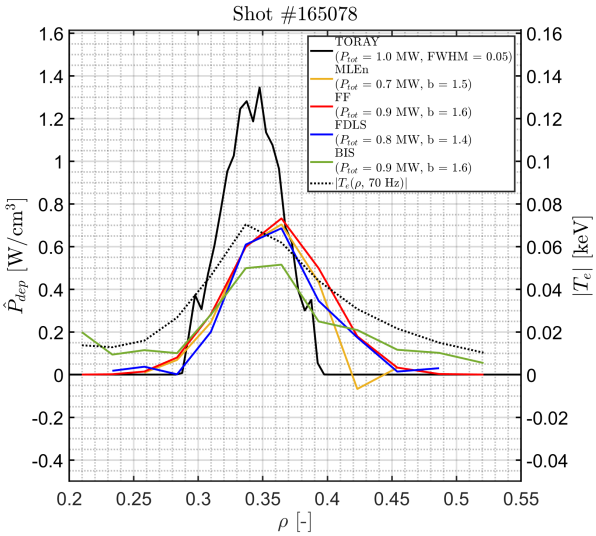

(B) DIII-D discharge 165078 (diverted L-mode, B_T = 2.0 T, I_p = 1.0 MA, $n_{e,0}$ = 2.9×10^{19} m^{-3}, P_{mECH} = 1.0 MW)

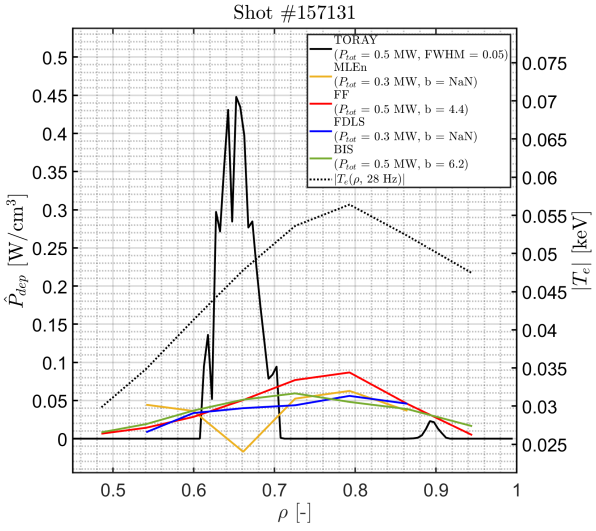

(C) DIII-D discharge 157131 (QH-mode, B_T = 1.9 T, I_p = 1.1 MA, $n_{e,0}$ = 1.7×10^{19} m^{-3}, P_{mECH} = 0.5 MW)

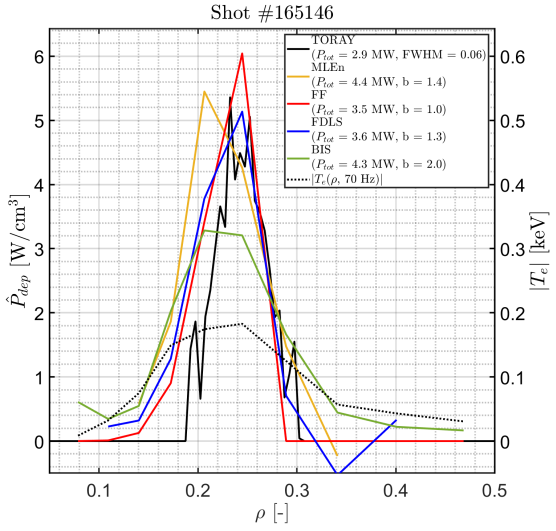

(D) DIII-D discharge 165146 (ELMy H-mode, B_T = 2.0 T, I_p = 1.0 MA, $n_{e,0}$ = 3.2×10^{19} m^{-3}, P_{mECH} = 2.9 MW)

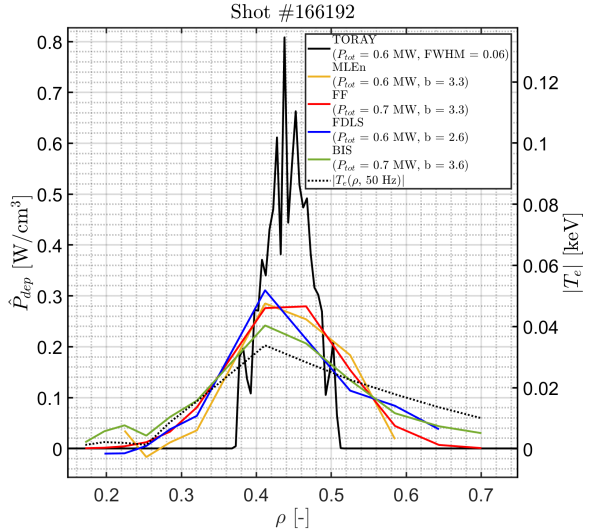

(E) DIII-D discharge 166192 (negative triangularity L-mode, B_T = 2.0 T, I_p = 0.9 MA, $n_{e,0}$ = 3.0×10^{19} m^{-3}, P_{mECH} = 0.6 MW)

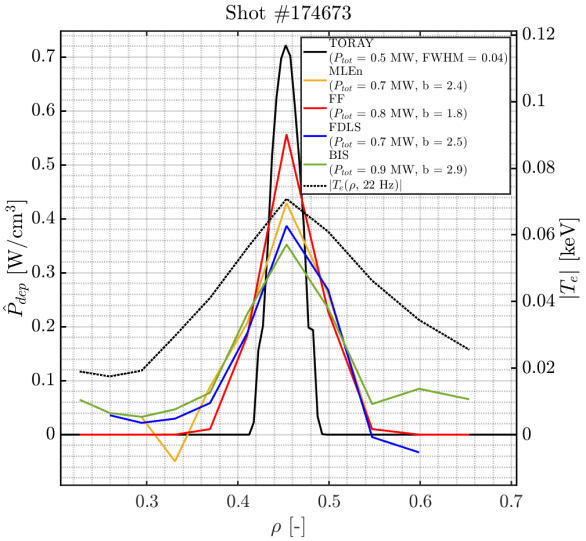

(F) DIII-D discharge 174673 (QH-mode, B_T = 2.0 T, I_p = 1.1 MA, $n_{e,0}$ = 3.2×10^{19} m^{-3}, P_{mECH} = 0.6 MW)

FIGURE 5.4: Power deposition estimates

TABLE 5.2: Summary of table 5.1, indicating for each discharge the FWHM of the TORAY-GA estimate (in the dimensionless coordinate ρ), the range of broadening according to (5.2) resulting from the four other estimation methods (MLE, FDLS, FF, MLE), the total deposited power according to the TORAY-GA estimate and the injected power from the four other estimation methods.

	FWHM TORAY [-]	b (min - max)	P_{tot} TORAY [MW]	P_{tot} other (min - max) [MW]
Limited L-mode (154532)	0.10	1.6-1.8	2.7	2.6-3.1
Diverted L-mode (165078)	0.05	1.4-1.6	1.0	0.7-0.9
QH-mode (157131)	0.05	4.4-6.2	0.5	0.3-0.5
QH-mode (174673)	0.06	1.8-2.9	0.5	0.7-0.9
ELMy H-mode (165146)	0.06	1.0-2.0	2.9	3.5-4.4
-δ L-mode (166192)	0.04	2.6-3.6	0.6	0.6-0.7

and 165146 in the deposition peaks, but even in those discharges the other points of the profiles agree quite well.

The broadening factor b agrees well among the methods for the limited and diverted L-mode discharges, while in the other discharges three out of four methods tend to agree well with one deviating somewhat. Comparing with b from [27], only some agreement is found for the ELMy H-mode discharge, while all other discharges find values for b that differ significantly. For two discharges, the broadening is observed here is less than in [27], likely due to the added freedom in peak location and/or profile shape in the methods used in this work (see section 3.3). In discharges 157131 and 166192, the broadening b reported here is significantly larger than in [27]. The reason for this is unclear. It could be that different EFIT and/or TORAY versions have been used, which (from experience) can vary quite significantly. The low power densities in 157131 are not unexpected given the low level of injected power and the proximity of deposition to the edge, where the flux tubes envelop a large volume.

The total injected power P_{tot} is computed through a (cylindrical) integral of the estimated deposition profiles, including the TORAY-GA one. Given the coarse spacing between the estimation points, this introduces some significant errors in the estimation of P_{tot}. This is likely why some discrepancies between the TORAY P_{tot} and the other estimation methods is seen, up to roughly 30%, though most estimations agree to a better degree than that. A notable exception is discharge 165146, with deviations in total absorbed power up to 50 %, though this is likely still attributable to the coarse integration grid as the profiles do not differ that significantly from the TORAY profile in this discharge. The non-TORAY estimations have only two points in the peak, so any deviations in those points lead to large deviations in the estimate of total injected power. Despite this, in absence of uncertainty estimates, the generally good agreement of total absorbed power between methods is a good indication that the estimations are reliable.

5.4 Scaling of broadening

The a priori plan for this work was to postulate a broadening mechanism and to experimentally test this hypothesis in a controlled experiment where a single variable is changed and the effect of this parameter on the resulting broadening is tested. Given, however, that what is available for analysis consists of a limited set of discharges that spans different regimes (i.e. different confinement modes, steady-state densities and temperatures etc.), it is nevertheless chosen to look for trends. This is done by comparing the observed broadening to the available set of parameters, which includes peak power location (in ρ), and the electron density and temperature for each discharge as a function of ρ.

Figure 5.5 shows the broadening factor b as defined in (5.2) as a function of the peak deposition location in ρ, for each of the 6 analyzed discharges and for each of the 4 estimation methods per discharge, with the exception of discharge 157131, for which for two of the methods it was not possible to define a broadening

factor. These are recognized as the rightmost two points in the figure.

First, it can be seen that the break-in-slope method systematically shows the most broadening out of the four methods. Second, the FDLS and MLE methods lie very close to each other in their estimations, which is somewhat surprising given their different assumptions (locally-constant parameters versus continuous functions). Third, the figure hints at an approximately linear correlation between broadening and increasing radius. If true, this would imply that power deposited near the plasma edge (either at the high- or low-field side of the plasma, something that cannot be discerned from figure 5.5) tends to get broadened more than power deposited near the core.

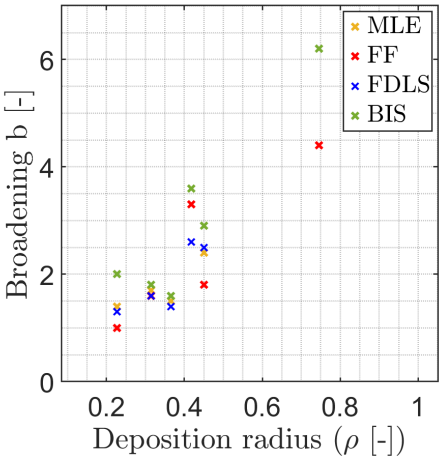

FIGURE 5.5: The ECH power deposition broadening as defined in (5.2) shows a positive correlation with peak power deposition radius in ρ for DIII-D discharges (from left to right): 165146, 154532, 165078, 166192, 174673 and 157131, for four different estimation methods per discharge. Discharge 157131 has only two points since for two estimations it was not possible to define a FWHM, others have three where points overlap.

Three other possible scalings are investigated, based on available measurement data: electron temperature $T_e(\rho)$ and electron density $n_e(\rho)$, measured with ECE and Thomson scattering. No clear relation is observed between broadening and either temperature or density at the peak power deposition location. The same is not true for their product; figure 5.6 shows the broadening factor b as defined in 5.2 as a function of $1/n_eT_e$ at the location of peak power deposition. The figure hints at a negative correlation between the observed broadening and the electron pressure at the peak power deposition location. This could indicate a possible pressure-induced or pressure-related physical process that plays a role in the broadening.

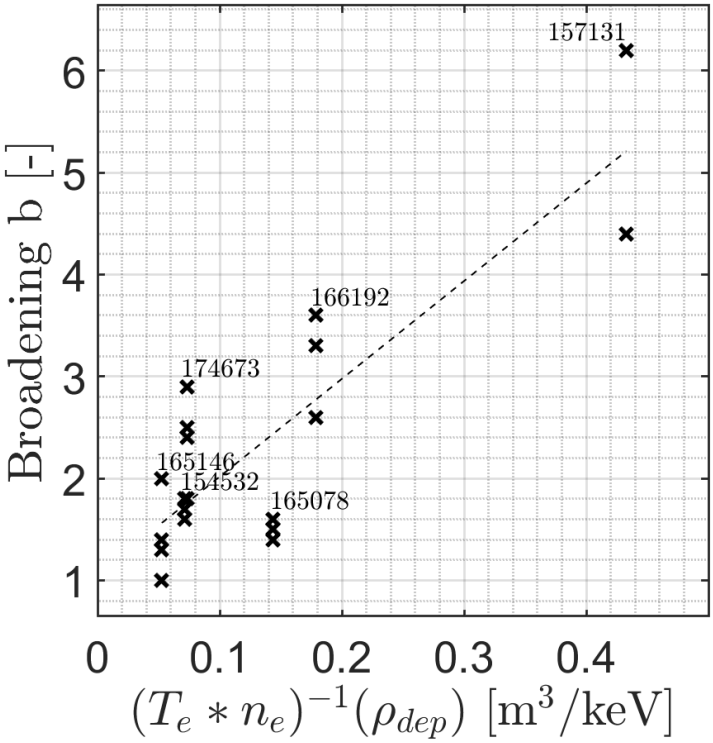

FIGURE 5.6: The ECH power deposition broadening as defined in (5.2) shows a weak negative correlation with electron pressure (proportional to the product of electron temperature T_e and density n_e) at the peak deposition location, indicated by the dashed line, across DIII-D discharges with different experimental conditions. Discharge numbers are indicated in the figure. The different points (stacked horizontally) indicate the different estimation methods per discharge.

Chapter 6

Summary, Discussion and Outlook

In this chapter, a summary of the work presented in all preceding chapters will be given, before discussing the results from those chapters. The discussion will revolve around the simulation results, the observed correlations and uncertainty analysis.

6.1 Summary

In summary, the ECH power deposition profile is estimated using five different estimation methods based on electron temperature and density measurements from DIII-D perturbative experiments, and compared to ray tracing profiles for a set of six discharges with different confinement modes and experimental conditions. Two of these methods, the maximum likelihood estimator (MLE) and the frequency domain least squares (FDLS) estimator, have readily available implementations. The other three, namely the Fast Fourier Transform (FFT), the break-in-slope (BIS), and flux fit (FF) methods, are implemented in this work based on the available literature. The flux fit method is adapted from the method presented in [27]. It is shown that the original flux fit method in [27], with a single parameter describing the deposition profile, does not contain enough freedom to accurately estimate the deposition profile in all cases. The adapted method, presented in this thesis, increases the number of parameters describing the deposition profile to four, increasing the freedom and the accuracy in the deposition profile estimation.
As a validation step, the methods are applied to simulations of perturbative experiments, before being applied to measurement data from six DIII-D discharges to estimate the power deposition profile and quantify the broadening of the resulting profiles compared to TORAY-GA estimates for each of these discharges. The assumptions of non-perturbed density and linearity are discussed based on two specific discharges with the right experimental conditions. Finally, the observed broadening from the six different discharges with different regimes is plotted against deposition radius and electron pressure to investigate possible scalings of broadening across the different discharges.

6.2 Simulations

From simulations of perturbative experiments it was concluded that the MLE, FF and FDLS methods perform the best in estimating the power deposition profile, especially in noisy conditions. It was found (not shown) that FF and FDLS methods, specifically, generally performed the best. This is not surprising given that both of those methods estimate smooth profiles where smooth profiles were simulated. Real effects like e.g. wall-reflections, potentially causing significant absorption in unexpected regions of the plasma, were not taken into account. In such circumstances, the MLE with its local, point-wise parameter estimation might perform better than e.g. the FF method.

It was also found that the FFT and BIS estimates were broadened under the chosen circumstances, which relates to the chosen levels of transport and the modulation frequency. While these conclusions are valid within the context of this work, since these parameters were chosen to be close to the circumstances in

the DIII-D discharges that were subsequently analyzed, that does not mean that the FFT and BIS are not great tools in different circumstances such as when transport is intrinsically low or when modulation frequencies are much higher.

6.3 Measurement channel spacing

The spacing for the DIII-D ECE channels determines the spacing for the deposition profile estimations. From the results in figure 5.4 it can be seen that, especially for certain discharges like 165146 and 157131, the spacing is too course to really obtain accurate profiles. This leads to uncertainty in the estimated broadening factor (as well as in the estimate of total absorbed power). Since it is not know what type of interpolation between the estimated points in the deposition profiles fits best, a simple linear interpolation is used for the curves in figure 5.4 which introduces errors in the determination of the FWHM of the curves. Fitting e.g. a Gaussian curve through the estimation points could reduce the observed broadening somewhat (like for the FF estimation in 165146) but this is not a justified assumption, merely a practical consideration. A better solution to this problem could be to fit splines through the estimated points, which leads to a smoother profile than linear interpolation but does not assume a predefined curve shape to the extent that a Gaussian fit would. Implementing this will be a good extension to the present work.

Another solution would be to perform new perturbative experiments with tighter spaced, variable location ECE channels [53, 84] that have been installed in the DIII-D tokamak after the discharges analyzed in this work were made. In new experiments, the variable location channels, which can be spaced together as closely as 0.6-0.8 cm [53] in contrast to the current 1-3 cm spacing, could be centered as tightly as possible around the deposition region to obtain estimated profiles with a finer spatial resolution. This, in turn, could lead to more precise broadening estimates and reduce to some extent the uncertainty due to the current linear interpolation.

6.4 Scaling with edge density fluctuation amplitude

In literature, it has been shown that rapid plasma edge density fluctuations can scatter ECH beams, resulting in a broadened deposition profile [18, 22, 26, 85, 86]. In [27] a scaling of broadening with edge density fluctuation amplitude was proposed. The latter was measured using Doppler Back Scattering (DBS), obliquely launching radiation into the plasma edge and measuring the Doppler broadening of the scattered radiation. While the same discharges were analyzed in this work and in [27], access to the DBS data could not be obtained. Hence, it has not yet been possible to test that scaling using the methods presented in this thesis, which differ from those in [27]. Recreating the scaling proposed in [27], either by obtaining access to the DBS measurements for the discharges analyzed in [27] and in this thesis or by analyzing a new set of discharges and including DBS measurements, will be one of the most important next steps for this research.

6.5 Scaling of broadening with radius and pressure

No sources were found in literature that analyze ECH deposition broadening as a function of deposition radius. The results in figure 5.5 can therefore not directly be compared. However, these results seem counter to the edge density scattering hypothesis in e.g. [27], based on the following: given the injection geometry and the low-field side ECH resonance location (figure 2.6), and assuming predominantly single-pass absorption, it would seem that deposition further away from the source of scattering (the edge), i.e. closer to $\rho = 0$, would lead to more significant broadening. This is exactly the opposite of what figure 5.5 shows. While it is possible that, purely coincidentally, the peak deposition location happens to coincide with edge density fluctuation amplitude across the discharges in figure 5.5 (which could not be checked,

see section 6.4), it is also possible that the observed correlation is an indication of significant double-pass absorption or some other absorption-related effect.

In addition to the above, evidence is presented in figure 5.6 for a negative correlation between ECH beam broadening and electron pressure. Admittedly, the evidence presented is weak; uncertainties on the broadening nor on temperature nor on density are taken into account, not all data points fit the linear trend well (discharge 165078 is a notable exception) and the data points from discharge 157131 are somewhat of an outlier. If the latter points are removed the trend becomes much less clear. Moreover, the data points in the figure stem from discharges with very different experimental conditions, so other parameters that have not been investigated may explain the broadening. In addition to performing a full uncertainty analysis and adding uncertainty bounds to figure 5.6 (see next section), the following is proposed to verify the results in figure 5.6 in the hypothetical scenario that this research could be extended by several months and that it will include the opportunity to perform a set of discharges in e.g. DIII-D:

Perform a number of discharges with power deposited evenly spaced in ρ spanning most of the range between core and edge (e.g. five discharges with deposition at $\rho \approx 0.2, 0.35, 0.5, 0.65, 0.8$), and do this separately for two different confinement modes. Preferably these modes differ as much as possible, especially in edge density fluctuation amplitude, e.g. a limited or diverted L-mode and a negative triangularity L-mode or QH-mode (see [27]). Make sure the power level is significant (> 1 MW, preferably closer to 3 MW) and the modulation rate f_0 is relatively slow (≤ 40 Hz, but larger than the reciprocal energy confinement time $1/\tau_E$) so as to be able to access time-resolved density measurements using either Thomson scattering or reflectrometry or both. This would allow the testing of the non-perturbed density assumption for every discharge in the experiment. Make sure that the modulation period $1/f_0$ is an integer multiple of both the ECE sample period $1/f_{s,ECE}$ and the ECH modulation sample period $1/f_{s,MECH}$. It might even be possible to change the injected power level (while keeping the modulation frequency constant) by some constant factor sometime during each discharge, if this is technologically possible, to allow checking the linearity assumption for every discharge. It is imperative to make sure that all gyrotron settings (injected power, modulation frequencies) are kept constant over all ten discharges with the exception of the approximate deposition location and potentially the step in power level, which should be the same at the same time for each discharge. Enable the DBS diagnostic to measure edge density fluctuation amplitude. All of this, taken together, would allow:

- Recreation of figure 5.5 at five different plasma locations spanning the plasma between core and edge, independent of plasma confinement mode, for two different confinement modes, which moreover correspond to the highest and lowest DBS fluctuation amplitudes $\tilde{n}_{e,DBS}$.
- In the same way a recreation of figure 5.6, and potentially the creation of a similar result for b vs. $\tilde{n}_{e,DBS}$.
- Checking the non-perturbed density and linearity assumptions for each discharge analyzed.

6.6 Uncertainty

A good check of the estimated profiles, in absence of error bars, is the estimate of total power injected. This should at any rate not be larger than what is injected, and not significantly lower, either. Comparing the four different methods again offers a sanity check to filter out unreliable estimates. However, purely based on the assumed uncertainties in T_e and ρ and the coarse grid spacing, it is not unreasonable to expect uncertainties on the order of up to 30 % in the total estimated power.

The uncertainty analysis that was performed in the work, such as seen in the simulation estimations in section 4.1.1, is mostly based on fitting errors. The FDLS method method estimates a fitting error for each spatial point in the estimated power deposition profile based on the fit residual. The BIS method

does the same using the fit residuals of the slope fits at each spatial location. The FF method uses the fit residual for the four fit parameters in the parametrization of the deposition profile. It is assumed that the uncertainties in each of these parameters are independent of each other, and therefore simply added, when in reality they are non-linearly dependent on each other. For example, since the parametrization is based on a Gaussian, uncertainties in the width and height of the overall profile both result in a similar uncertainty on the power deposited at a single spatial estimation location. In the future, these dependent uncertainties will be handled using nonlinear propagation of uncertainty, i.e. by Taylor expanding the fit function to first order in the fit parameters and thereby defining the uncertainty in the overall function based on the uncertainties in the estimated parameters [87].

Only the MLE takes a measure of uncertainty on the measurement data (specifically, T_e) into account by estimating the variance of that data over multiple periods. This is done based on the assumption of normal complex circular distributed (NCCD) noise [28]. None of these methods, however, are currently able to take the systematic measurement uncertainties (e.g. calibration errors) on the measured quantities (T_e and n_e) into account. Hence, it was decided that error bars based only on fitting errors do not paint an accurate enough picture of the true uncertainty in the estimates (unlike the simulated cases where there is no uncertainty on the "measurements") and therefore it was chosen to present the results without uncertainty bounds. While the magnitude of the systematic and calibration errors in ECE and Thomson scattering measurements of T_e and n_e are known (e.g. for ECE measurements the error is assumed to be on the order of 5 % based on experience with the set-up), one would also like to know the distribution of the errors (Gaussian, uniform, ...) in order to be accurately incorporated in the estimation. In absence of this information, at least the estimated systematic uncertainty in the measured quantities can be taken into account by implementing e.g. Total Least Squares (TLS) or Orthogonal Distance Regression (ODR) to replace the (non)linear least square methods used currently in the fitting procedure in the FDLS, FF and BIS methods.

An even more complete uncertainty analysis could include the horizontal uncertainty in ρ, which is typically assumed to be on the order of 2-3 %. The mapping of measurements to ρ involves equilibrium reconstruction based on a complex interplay of diagnostic information, so the precise uncertainty is unknown. Quantifying this uncertainty is possible through a sensitivity analysis of the equilibrium reconstruction routine used, in this case EFIT. Taking the uncertainty in ρ into account without drastically overestimating the total uncertainty is complicated, however, by the fact that its uncertainty is not independent of the uncertainty in the measured quantities (T_e and n_e), so this would again require a nonlinear propagation of uncertainty approach to correctly take the interdependency of the measurements and ρ into account. If not done carefully, this could lead to an unrealistically large uncertainty estimate, which would diminish the ability to conclude from any obtained results.

6.7 Impact on NTM stabilization

One of the most important applications for the injection of electron cyclotron (EC) waves into tokamak plasmas is the stabilization of neoclassical tearing modes (NTMs), especially in large, future devices like ITER [16, 88–90]. In a 2015 study by Poli et al. [91], it was found that the EC power installed in ITER will be sufficient to stabilize NTMs if absorption profiles follow the predictions by ray tracing. Assuming a marginal island width (the width at which the NTM magnetic island self-stabilizes, i.e. stops growing) of 1-2 cm, it was found that this will still be the case up to a deposition broadening compared to ray tracing of two. If the deposition is broadened by more than that, continuous ECCD will not be sufficient to stop islands of that size from growing.
Given the level of broadening reported in this work, depending on how the experimental conditions in the DIII-D discharge that were analyzed compare to those in ITER, this may have implications for the ITER NTM stabilization system. In case the ITER conditions will be similar to e.g. DIII-D discharge 154532, 165078 or 165146, where the reported broadening is below 2, nothing will change in the ITER

design. In the cases of discharges 166192 and 174673, with broadening between 2 and 3.5 times, NTM stabilization in ITER may require pulsed ECCD, rather than continuous operation. Alternatively, the injection angle may be decreased to increase current drive efficiency, at the cost of reaching deeper layers of the plasma. If the broadening in ITER will be as severe as in DIII-D discharge 157131, there may simply not be enough EC power in ITER to stabilize NTMs based on the findings in [91]. Given that the positive correlation between broadening and deposition radius reported in this thesis, and that EC power deposition for NTM suppression in ITER will be located close to the edge ($\rho > 0.7$)[91], the latter scenario might be the case. However, if the negative correlation with pressure dominates the broadening effect, the higher temperatures and densities in ITER compared to DIII-D [92] might negate the broadening effect. It must therefore be investigated how the results in this thesis translate to ITER.

Chapter 7

Conclusion

Five different methods for estimating ECH power deposition profiles based on experimental data are tested on simulated data before being applied to DIII-D measurement data and compared to TORAY estimates to resolve the discrepancy that has been previously observed between experimental and theoretical (ray tracing) power deposition estimates. From this, the following is concluded:

1) The BIS and FFT methods are not the most suitable power deposition profile estimation methods for the conditions such as they are found in the DIII-D discharges that were analyzed (i.e. diffusivity < 10 m^2/s and modulation frequency < 100 Hz), based on the simulations that were performed. In contrast, the MLE, FDLS and FF methods perform well in estimating the deposition profile in the simulated conditions. Additionally, based on the same simulations, in noisy conditions such as they are always found in real experiments, the diffusivity cannot be accurately estimated using the methods used. However, this does not influence the accuracy of the power deposition estimates

2) Based on the analysis of DIII-D discharges, it was concluded that the deposition profiles estimated using the experimental methods presented in this thesis are significantly broadened with respect to the TORAY-GA estimates, by between one and six times depending on the discharge and the method (but mostly between one-and-a-half to three times).

3) Finally, there is preliminary evidence that the observed broadening scales positively with deposition radius and negatively with electron pressure at the deposition location. This should be further investigated in future work.

Bibliography

1. BIPM. *Le Système international d'unités / The International System of Units ('The SI Brochure')* 9th edition. ISBN: 978-92-822-2272-0 (Bureau international des poids et mesures, 2019).
2. NIST. 2018 CODATA Value: electron mass. *The NIST Reference on Constants, Units, and Uncertainty* (2019).
3. NIST. 2018 CODATA Value: proton mass. *The NIST Reference on Constants, Units, and Uncertainty* (2019).
4. NIST. 2018 CODATA Value: vacuum electric permittivity. *The NIST Reference on Constants, Units, and Uncertainty* (2019).
5. IEA. *World Energy Outlook 2019* technical report (IEA, Paris, 2019).
6. Masson-Delmotte, V. *et al. Global Warming of 1.5°C. An IPCC Special Report on the impacts of global warming of 1.5°C above pre-industrial levels and related global greenhouse gas emission pathways, in the context of strengthening the global response to the threat of climate change, sustainable development, and efforts to eradicate poverty* technical report (IPCC, 2018).
7. Prater, R. Heating and current drive by electron cyclotron waves. *Physics of Plasmas* **11,** 2349–2376 (2004).
8. Pinsker, R. I. Introduction to wave heating and current drive in magnetized plasmas. *Physics of Plasmas* **8,** 1219–1228 (2001).
9. Fisch, N. Theory of current drive in plasmas. *Reviews of Modern Physics* **59,** 175–234 (1987).
10. Ryter, F. *et al.* Electron heat transport in ASDEX Upgrade: experiment and modelling. *Nuclear Fusion* **43,** 1396–1404 (2003).
11. Zerbini, M. *et al.* Correlation analysis of 110 GHz ECH modulation experiments on the DIII-D tokamak. *Plasma Physics and Controlled Fusion* **41,** 931–940 (1999).
12. Lopes Cardozo, N. J. Perturbative transport studies in fusion plasmas. *Plasma Physics and Controlled Fusion* **37,** 799–852 (1995).
13. Hoshino, K. & Takahashi, K. Suppression of the m/n=2/1 tearing mode by ECH/ECCD on JFT-2M Tokamak. *Fusion Engineering and Design* **53,** 249–257 (2001).
14. Luce, T. Applications of high-power millimeter waves in fusion energy research. *Plasma Science, IEEE Transactions on* **30,** 734–754 (2002).
15. Esposito, B. *et al.* Disruption control on FTU and ASDEX upgrade with ECRH. *Nuclear Fusion* **49,** 065014 (2009).
16. La Haye, R. J. Neoclassical tearing modes and their control. *Physics of Plasmas* **13,** 55501 (2006).
17. Erckmann, V. & Gasparino, U. Electron cyclotron resonance heating and current drive in toroidal fusion plasmas. *Plasma Physics and Controlled Fusion* **36,** 1869–1962 (1994).
18. Decker, J., Peysson, Y. & Coda, S. Effect of density fluctuations on ECCD in ITER and TCV. *EPJ Web of Conferences* **32,** 01016 (2012).
19. Kirov, K. K. *et al.* ECRH power deposition studies in ASDEX Upgrade. *Plasma Physics and Controlled Fusion* **44,** 2583–2602 (2002).
20. Van Berkel, M. *et al.* Heat flux reconstruction and effective diffusion estimation from perturbative experiments using advanced filtering and confidence analysis. *Nuclear Fusion* **58,** 096036 (2018).
21. Gentle, K. W., Austin, M. E., DeBoo, J. C., Luce, T. C. & Petty, C. C. Electron energy transport inferences from modulated electron cyclotron heating in DIII-D. *Physics of Plasmas* **13,** 012311 (2006).

22. Brookman, M. W., Austin, M. E. & Petty, C. C. Finding evidence for density fluctuation effects on electron cyclotron heating deposition profiles on DIII-D. *AIP Conference Proceedings* **1689,** 090005 (2015).
23. Brookman, M. *et al.* Resolving ECRH deposition broadening due to edge turbulence in DIII-D by heat deposition measurement. *Physics of Plasmas* **28** (2017).
24. Köhn-Seemann, A. *et al.* The deteriorating effect of plasma density fluctuations on microwave beam quality. *EPJ Web of Conferences* **203** (2019).
25. Thomas, M. *et al.* Resolving ECRH deposition broadening due to edge turbulence in DIII-D by 3D full-wave simulations (2017).
26. Brookman, M. *et al.* Experimental Measurement of ECH Deposition Broadening: Beyond Anomalous Transport. *EPJ Web of Conferences* **147,** 03001 (2017).
27. Brookman, M. W. *et al.* Resolving ECRH deposition broadening due to edge turbulence in DIII-D. *Physics of Plasmas* **28,** 042507 (2021).
28. Van Berkel, M. *Estimation of heat transport coefficients in fusion plasmas* PhD thesis (Department of Mechanical Engineering, 2015).
29. Van Berkel, M. *et al.* Frequency domain sample maximum likelihood estimation for spatially dependent parameter estimation in PDEs. *Automatica* **50,** 2113–2119 (2014).
30. Das, A., Weiland, S. & Van Berkel, M. Frequency Domain Estimation of Spatially Varying Parameters in Heat and Mass Transport. *Proceedings of the 2019 American Control Conference,* 600–605 (2019).
31. Van Berkel, M., Oosterwegel, G. W., Anthonissen, M., Zwart, H. J. & Vandersteen, G. A novel frequency domain maximum likelihood approach for estimating transport coefficients in cylindrical geometry for nuclear fusion devices. *Proceedings of the IEEE Conference on Decision and Control* **58,** 3220–3226 (2019).
32. Van Kampen, R. J. R., Das, A., Weiland, S. & Van Berkel, M. A Closed-Form Solution to Estimate Spatially Varying Parameters in Heat and Mass Transport. *IEEE Control Systems Letters* **5,** 1681–1686 (2021).
33. Gamow, G. Zur Quantentheorie des Atomkernes. *Zeitschrift für Physik* **51,** 204–212 (1928).
34. Freidberg, J. P. *Plasma Physics and Fusion Energy* (Cambridge University Press, 2007).
35. Hoshino, T. *et al.* Development of advanced tritium breeding material with added lithium for ITER-TBM. *Journal of Nuclear Materials* **417,** 684–687 (2011).
36. Ongena, J. & Ogawa, Y. Nuclear fusion: Status report and future prospects. *Energy Policy* **96,** 770–778 (2016).
37. Shafranov, V. On the history of the research into controlled thermonuclear fusion. *Journal of the Russian Academy of Sciences* **44,** 835–865 (2001).
38. Pitts, R., Buttery, R. & Pinches, S. Fusion: the way ahead. *Physics World* **19,** 20–26 (2006).
39. Grad, H. & Rubin, H. *Hydromagnetic equilibria and force-free fields* in *Proceedings of the Second United Nations International Conference on the Peaceful Uses of Atomic Energy* (United Nations, Geneva, 1958), 190–197.
40. Brix, M., Hawkes, N. C., Boboc, A., Drozdov, V. & Sharapov, S. E. Accuracy of EFIT equilibrium reconstruction with internal diagnostic information at JET. *Review of Scientific Instruments* **79,** 10F325 (2008).
41. Furth, H. P., Killeen, J. & Rosenbluth, M. N. Finite-resistivity instabilities of a sheet pinch. *Physics of Fluids* **6,** 459–484 (1963).
42. Hegna, C. C. & Callen, J. D. Stability of tearing modes in tokamak plasmas. *Physics of Plasmas* **1,** 2308–2318 (1994).
43. Bardóczi, L., Carter, T. A., La Haye, R. J., Rhodes, T. L. & McKee, G. R. Impact of neoclassical tearing mode–turbulence multi-scale interaction in global confinement degradation and magnetic island stability. *Physics of Plasmas* **24,** 122503 (2017).
44. Schuller, F. C. Disruptions in tokamaks. *Plasma Physics and Controlled Fusion* **37,** A135–A162 (1995).

45. Maraschek, M. *et al.* Active control of MHD instabilities by ECCD in ASDEX Upgrade. *Nuclear Fusion* **45,** 1369–1376 (2005).
46. Günter, S. *et al.* Neoclassical tearing modes on ASDEX upgrade: Improved scaling laws, high confinement at high βN and new stabilization experiments. *Nuclear Fusion* **43,** 161–167 (2003).
47. Chen, F. F. *Introduction to Plasma Physics and Controlled Fusion* 3rd edition. ISBN: 978-3-319-22308-7 (Springer International Publishing, 2016).
48. Luxon, J. L. A design retrospective of the DIII-D tokamak. *Nuclear Fusion* **42,** 614–633 (2002).
49. Bornatici, M., Cano, R., Barbieri, O. D. & Engelmann, F. Electron cyclotron emission and absorption in fusion plasmas. *Nuclear Fusion* **23,** 1153–1257 (1983).
50. Westerhof, E. *Electron cyclotron waves, transport and instabilities in hot plasmas* PhD thesis (Utrecht University, 1987).
51. Evans, T. E. Implications of topological complexity and hamiltonian chaos in the edge magnetic field of toroidal fusion plasmas. *Chaos, Complexity and Transport* **1,** 147–176 (2008).
52. Peters, M., Gorini, G. & Mantica, P. Optical thickness corrections to transient ECE temperature measurements in tokamak and stellarator plasmas. *Nuclear Fusion* **35,** 873–875 (1995).
53. Truong, D. D. & Austin, M. E. High spatial resolution upgrade of the electron cyclotron emission radiometer for the DIII-D tokamak. *Review of Scientific Instruments* **85,** 11D814 (2014).
54. *https://fusion.gat.com/global/diii-d/home* (2020).
55. Cengher, M. *et al.* DIII-D Electron Cyclotron Heating System Status and Upgrades. *IEEE Transactions on Plasma Science* **44,** 3465–3470 (2016).
56. Cengher, M. *et al.* Status and Plans for the DIII-D ECH/ECCD System. *IEEE Transactions on Plasma Science* **48,** 1698–1702 (2020).
57. Boivin, R. L. *et al.* DIII-D diagnostic systems. *Fusion Science and Technology* **48,** 834–851 (2005).
58. Carlstrom, T. N. *et al.* Design and operation of the multipulse Thomson scattering diagnostic on DIII-D. **63,** 4901–4906 (1992).
59. Greenfield, C. M. *et al.* Real-time digital control, data acquisition, and analysis system for the DIII-D multipulse Thomson scattering diagnostic. *Review of Scientific Instruments* **61,** 3286–3288 (1990).
60. Thomson, J. J. *Conduction of Electricity through Gases* (Cambridge University Press, 1906).
61. Austin, M. E. & Lohr, J. Electron cyclotron emission radiometer upgrade on the DIII-D tokamak. *Review of Scientific Instruments* **74,** 1457–1459 (2003).
62. Wagner, F. *et al.* Development of an Edge Transport Barrier at the H-Mode Transition of ASDEX. *Physical Review Letters* **53,** 1453–1456 (1984).
63. Austin, M. E. *et al.* Achievement of Reactor-Relevant Performance in Negative Triangularity Shape in the DIII-D Tokamak. *Physical Review Letters* **122,** 115001 (2019).
64. Zohm, H. Edge localized modes (ELMs). *Plasma Physics and Controlled Fusion* **38,** 105–128 (1996).
65. Burrell, K. H. *et al.* Quiescent H-mode plasmas in the DIII-D tokamak. *Plasma Physics and Controlled Fusion* **44,** A253–A263 (2002).
66. Burrell, K. H. *et al.* Quiescent H-mode plasmas with strong edge rotation in the cocurrent direction. *Physical Review Letters* **102,** 155003 (2009).
67. Suttrop, W. *et al.* Study of quiescent H-mode plasmas in ASDEX Upgrade. *Plasma Physics and Controlled Fusion* **46,** A151–A156 (2004).
68. Hogeweij, G. M. D. *et al.* Studies of transport in the RTP tokamak. *Physica Scripta* **51,** 627–631 (1995).
69. Hogeweij, G. M. D. Transport studies using perturbative experiments. *Fusion Science and Technology* **45,** 315–320 (2004).
70. Efthimion, P. C. *et al.* Comparison of steady-state and perturbative transport coefficients in TFTR. *Physics of Fluids B: Plasma Physics* **3,** 2315–2323 (1991).
71. Lang, P. *et al.* ELM control strategies and tools: Status and potential for ITER. *Nuclear Fusion* **53,** 043004 (2013).
72. Lerche, E. A. & and, D. V. E. Improved break-in-slope analysis of the plasma energy response in tokamaks. *Plasma Physics and Controlled Fusion* **50,** 035003 (2008).

73. Heideman, M., Johnson, D. & Burrus, C. Gauss and the history of the fast Fourier transform. *Archive for History of Exact Sciences* **34,** 265–277 (1985).
74. Myung, I. J. Tutorial on maximum likelihood estimation. *Journal of Mathematical Psychology* **47,** 90–100 (2003).
75. Prater, R. *et al.* Benchmarking of codes for electron cyclotron heating and electron cyclotron current drive under ITER conditions. *Nuclear Fusion* **48,** 035006 (2008).
76. Harris, F. On the use of windows for harmonic analysis with the discrete Fourier transform. *Proceedings of the IEEE* **66,** 51–83 (1978).
77. Pintelon, R., Schoukens, J., Vandersteen, G. & Barbé, K. Estimation of nonparametric noise and FRF models for multivariable systems-Part I: Theory. *Mechanical Systems and Signal Processing* **24,** 573–595 (2010).
78. Pintelon, R., Schoukens, J., Vandersteen, G. & Barbé, K. Estimation of nonparametric noise and FRF models for multivariable systems-Part II: Extensions, applications. *Mechanical Systems and Signal Processing* **24,** 596–616 (2010).
79. Van Berkel, M. *et al.* Correcting for non-periodic behaviour in perturbative experiments: application to heat pulse propagation and modulated gas-puff experiments. *Plasma Physics and Controlled Fusion* **62,** 094001 (2020).
80. Van den Boorn, B. H. *Sensitivity analysis of the heat transport coefficient estimation in fusion reactors and their identifiability under noisy conditions* Master's thesis (Eindhoven University of Technology, 2021).
81. Hastie, R. J. Sawtooth instability in tokamak plasmas. *Astrophysics and Space Science* **256,** 177–204 (1997).
82. Weik, M. H. in *Computer Science and Communications Dictionary* 661–661 (Springer US, Boston, MA, 2001). ISBN: 978-1-4020-0613-5.
83. Weisstein, E. W. Gaussian Function. *MathWorld – A Wolfram Web Resource* (2021).
84. Xie, R., Houshmandyar, S. & Austin, M. E. Active control of electron cyclotron emission radiometer channel frequencies for improved electron temperature measurements. *Review of Scientific Instruments* **92,** 33530 (2021).
85. Köhn, A. *et al.* Microwave beam broadening due to turbulent plasma density fluctuations within the limit of the Born approximation and beyond. *Plasma Physics and Controlled Fusion* **60,** 075006 (2018).
86. Chellaï, O. *et al.* Millimeter-Wave Beam Scattering by Field-Aligned Blobs in Simple Magnetized Toroidal Plasmas. *Physical Review Letters* **120,** 105001 (2018).
87. Wang, C. M. & Iyer, H. K. On higher-order corrections for propagating uncertainties. *Metrologia* **42,** 406–410 (2005).
88. Hizanidis, K., Ram, A. K., Kominis, Y. & Tsironis, C. Fokker-Planck description of the scattering of radio frequency waves at the plasma edge. *Physics of Plasmas* **17,** 022505 (2010).
89. Henderson, M. A. *et al.* The Front Steering Launcher Design for the ITER ECRH Upper Port. *Journal of Physics: Conference Series* **25,** 143–150 (2005).
90. Van den Brand, H., de Baar, M. R., Lopes Cardozo, N. J. & Westerhof, E. Integrated modelling of island growth, stabilization and mode locking: consequences for NTM control on ITER. *Plasma Physics and Controlled Fusion* **54,** 094003 (2012).
91. Poli, E. *et al.* On recent results in the modelling of neoclassical-tearing-mode stabilization via electron cyclotron current drive and their impact on the design of the upper EC launcher for ITER. *Nuclear Fusion* **55,** 013023 (2015).
92. Ghendrih, P. *et al.* Collisions in magnetised plasmas. *ESAIM: Proceedings and Surveys* **50,** 81–112 (2015).